

## FULL SPECTRAL SURVEY OF ACTIVE GALACTIC NUCLEI IN THE ROSSI X-RAY TIMING EXPLORER ARCHIVE

ELIZABETH RIVERS<sup>1</sup>, ALEX MARKOWITZ<sup>1,2,3</sup>, RICHARD ROTHSCCHILD<sup>1</sup>

<sup>1</sup>University of California, San Diego, Center for Astrophysics and Space Sciences, 9500 Gilman Dr., La Jolla, CA 92093-0424, USA

<sup>2</sup>Dr. Karl Remeis Sternwarte, Sternwartstrasse 7, 96049 Bamberg, Germany and

<sup>3</sup>Alexander von Humboldt Fellow

*Draft version May 6, 2019*

### ABSTRACT

We have analyzed spectra for all active galactic nuclei in the *Rossi X-ray Timing Explorer (RXTE)* archive. We present long-term average values of absorption, Fe line equivalent width, Compton reflection and photon index, as well as calculating fluxes and luminosities in the 2–10 keV band for 100 AGN with sufficient brightness and overall observation time to yield high quality spectral results. We compare these parameters across the different classifications of Seyferts and blazars. Our distributions of photon indices for Seyfert 1's and 2's are consistent with the idea that Seyferts share a common central engine, however our distributions of Compton reflection hump strengths do not support the classical picture of absorption by a torus and reflection off a Compton-thick disk with type depending only on inclination angle. We conclude that a more complex reflecting geometry such as a combined disk and torus or clumpy torus is likely a more accurate picture of the Compton-thick material. We find that Compton reflection is present in  $\sim 85\%$  of Seyferts and by comparing Fe line EW's to Compton reflection hump strengths we have found that on average 40% of the Fe line arises in Compton thick material, however this ratio was not consistent from object to object and did not seem to be dependent on optical classification.

*Subject headings:* galaxies: active – X-rays: galaxies

### 1. INTRODUCTION

Active galactic nuclei (AGNs) are some of the most luminous objects in the universe, frequently outshining their host galaxies. Historically AGNs have been classified based on their optical and radio characteristics and were originally believed to be a variety of completely different objects. It is now thought that all AGNs share a common central engine: an accreting supermassive black hole (SMBH) located at the center of its host galaxy. Angle-dependance and obscuration can explain some of the observed differences in these objects but are not enough to explain the great variety of AGN properties that have been discovered.

AGNs display a wide variety of observed behaviors, making it difficult to place them neatly into categories. The most general distinction between AGN types is jet-dominated versus non jet-dominated. Blazars, which are radio bright with typically featureless continua, have particularly strong jet components which happen to be oriented along our line of sight. Therefore emission from the beamed jet dominates over disk/coronal emission from the central region of the AGN. The remaining categories of AGNs, Quasars, Seyferts, radio galaxies and low luminosity AGNs (LLAGNs), may have jets which are not beamed toward us or may have no jets at all. Quasars are very luminous, distant AGN while LLAGNs are much fainter and detected only nearby; however according to unification these objects may differ only in their masses and accretion rates. Optical observations are used to identify Seyfert 1's and broad line radio galaxies (BLRG's), which display broadened optical emission lines, versus Seyfert 2's and narrow line radio galaxies (NLRG's), which display only narrow emission lines. A special subset of Seyfert 1's are the so-called Narrow Line Seyfert 1's (NLSy1's) which display narrower broad emission lines than typical Seyfert 1's ( $H\beta_{\text{FWHM}} < 2000 \text{ km s}^{-1}$ ) and are thought to be relatively small SMBH's accreting very near the Edding-

ton limit with very steep (i.e. soft) X-ray spectra (see, e.g., Pounds et al. 1995; Grupe et al. 1999).

One thing that nearly all AGNs have in common is a strong X-ray component (Elvis et al. 1978). It is believed that the X-ray power law continuum arises very near the central black hole, either from the accretion disk itself or a hot corona surrounding the black hole, or in some cases possibly from the base of a launching jet. In addition to the continuum, Seyfert X-ray spectra can show a variety of components: emission lines (most commonly from Fe), absorption by gas which may be ionized (“warm”) or neutral (“cold”), an excess below about 2 keV known as the “soft excess,” and Compton reflection peaking around 20–30 keV in the hard X-ray spectrum. Seyfert 2's and NLRG's tend to have more absorption in the line of sight to the nucleus than Seyfert 1's (Antonucci et al. 1993), giving rise to the idea that we are seeing them “edge on” and that their broad line regions (BLR) exist but are hidden from view by the Compton-thick dusty torus which is seen in the infrared. This classical picture of Seyfert 1/2 unification is still up for debate however, with evidence to suggest that while they may share a central engine, differences in the geometry of the circumnuclear material including the accretion disk, corona, broad line region, and Compton-thick torus lead to the differences in observed characteristics that we see (see, e.g., Ramos Almeida et al. 2011). Placing tighter constraints on the geometry of this material may help unravel this mystery of Seyfert 1's and 2's.

The *Rossi X-ray Timing Explorer (RXTE)* performed numerous observations of AGNs over its 16-year lifespan in the energy range from 3 keV to 200 keV. This energy range is ideal for quantifying the underlying continuum parameters as well as measuring the Compton reflection hump (CRH), Fe  $K\alpha$  emission, and absorption by cold gas with column densities above  $\sim 10^{22} \text{ cm}^{-2}$ . We have performed detailed analysis of all AGNs in the *RXTE* archive for which high-quality spec-

tra could be obtained, totaling 100 objects in all. For many of these objects, continuous long-term monitoring data provides long-term baselines for quantities such as the continuum photon index ( $\Gamma$ ), the Compton reflection strength ( $R$ ) and the column density of absorbing material in the line of sight ( $N_{\text{H}}$ ). Relating these components gives us a clearer picture of the geometry of the circumnuclear material in Seyfert AGNs and allows us to test unification schemes.

This paper is a follow-up to Rivers et al. (2011; hereafter RMR2011) which analyzed 23 AGN spectra with a particular focus on high quality data from 20–100 keV, finding average values for the CRH strength, Fe line equivalent width ( $EW$ ), and photon index. This survey also found limited evidence for high energy rollovers below 100 keV (caused by the thermal shape of the corona not being able to produce many very high energy photons) with only two objects showing a significant rollover and ruling out the presence of a rollover in all but one of the other sources. We have quadrupled the sample size and include now all AGNs with high enough data quality to accurately measure  $\Gamma$ , as well as the CRH and Fe  $K\alpha$  line  $EW$  in most cases. The energy range for these spectra was from 3.5 keV up to at least 20 keV and as high as 200 keV for some objects. This sample will allow us to analyze the spectral components discussed above with an emphasis on bulk properties of different types of AGN, providing a test of the unified model. This paper is structured in the following way: Section 2 contains information on the *RXTE* archive and the data reduction process, Section 3 details analysis methods, and Section 4 contains a discussion of our findings.

## 2. ARCHIVAL OBSERVATIONS AND DATA REDUCTION

### 2.1. The *RXTE* Archive and Selection Criteria

The *RXTE* satellite made X-ray observations from 1996 January to 2012 January with its two pointed observation instruments, the Proportional Counter Array (PCA; Jahoda et al. 2006) and the High-Energy X-Ray Timing Experiment (HEXTE; Rothschild et al. 1998). In 16 years it observed 153 AGNs: 54 Seyfert 1’s, 47 Seyfert 2’s, and 52 Blazars, many of them multiple times. Note that we have included subtypes Seyfert 1.2 and 1.5 in with the Seyfert 1’s and Seyfert 1.8 and 1.9’s in with the Seyfert 2’s. The sampling of these objects has been highly inhomogeneous since different viewing schemes were proposed for each object at various times and for various scientific goals. We have included in our analysis all data for each object, regardless of sampling, in order to construct our overall averaged spectra.

We wanted to construct energy spectra of as many of these AGNs as possible, however several of these object were observed only once or twice for a handful of kiloseconds. It was therefore important for us to find the necessary conditions required to construct useful spectra. We decided to include a source in our sample if fitting the PCA data with a simple absorbed power law gave errors on the photon index of  $\lesssim 10\%$ . We included HEXTE data if the source was detected by HEXTE at the  $3\sigma$  level at 50 keV, otherwise only the PCA data were used. For the PCA we found that  $\sim 40,000$  total net counts was sufficient to give error bars of  $\lesssim 10\%$  on  $\Gamma$ . For HEXTE we found that  $\sim 5,500$  counts were necessary to detect the source at the  $3\sigma$  level at 50 keV, however the steepness of the spectrum was also a factor in general. For HEXTE, the whole energy range (20–250 keV) was used whenever the data were included, though in many cases it did not help to constrain the model fitting past  $\sim 50$ –100 keV. There were two

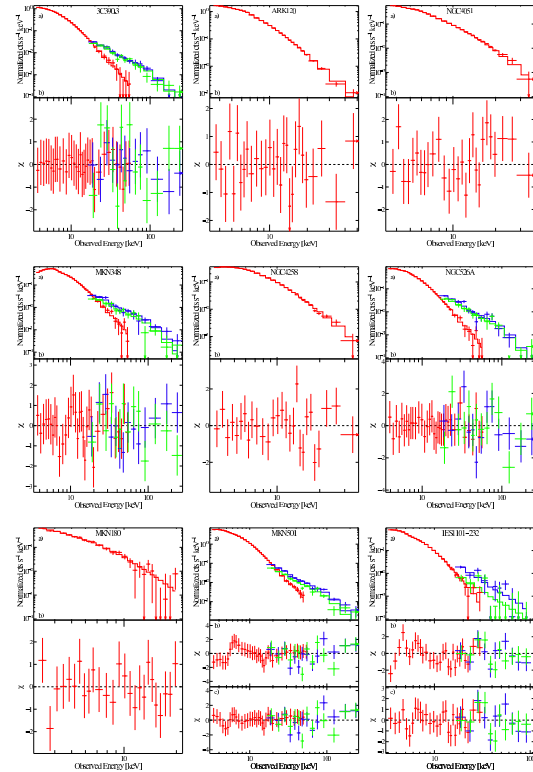


FIG. 1.— Data and data–model fit residuals for a small number of sources in our sample, chosen to display a range of poor to moderate data quality (note that no sources shown here have the highest data quality since those spectra were published in RMR2011). Panel (a) shows the data and best fit model, panel (b) shows the fit residuals to the base model (power law model for blazars), and when present, panel (c) shows the fit residuals to the best fit model (broken power law model for blazars). Parameters can be found in Tables 2–6. PCA data is in red while HEXTE A and B are blue and green, respectively. The top row are Seyfert 1’s, the middle row are Compton-thin Seyfert 2’s, and the bottom row are blazars.

exceptions which had significant background features around 100 keV that affected fitting and so were only included to 80–90 keV.

Using these selection criteria we constructed time-averaged spectra for 100 AGN. We identified these objects by their optical classifications per the NASA/IPAC extragalactic database (“NED”), dividing our sample into 34 blazars and 66 Seyferts, including 30 Seyfert 1’s, 10 Narrow Line Seyfert 1’s, and 26 Seyfert 2’s, 7 of which were Compton-thick (defined as  $N_{\text{H}} \geq 1 \times 10^{24}$ ). The names, redshifts, exposure times, and maximum energy included for each object in our sample are listed in Table 1. Those AGN in the archive which did not yield usable spectra are summarized in Appendix A.

### 2.2. Data Reduction

For all PCA and HEXTE data extraction and analysis we used HEASOFT version 6.7 software. Reduction of the data followed standard extraction and screening procedures as detailed in RMR2011. We used updated PCA background model files “pca\_bkgd\_cmvle\_eMv20111129.mdl” for source fluxes brighter than  $\sim 5$  mCrab, and “pca\_bkgd\_cmfaint7\_eMv20111129.mdl” for source fluxes fainter than  $\sim 5$  mCrab.

We extracted PCA STANDARD-2 data from PCU’s 0, 1

TABLE 1  
SOURCE LIST

Source Name	Type	W.A.	$z$	PCA	HEXTE	$E_{\max}$	Source Name	Type	$z$	PCA	HEXTE	$E_{\max}$
				(ks)	A, B (ks)	(keV)				(ks)	A, B (ks)	(keV)
3C 111	BLRG/Sy1		0.0485	1092	127, 278	40/250	Mkn 348	Sy2	0.0150	484	68, 59	60/250
3C 120	BLRG/Sy1		0.0330	2102	504, 629	40/250	NGC 526A	Sy2/NELG	0.0192	113	35, 34	60/250
3C 382	BLRG/Sy1		0.0579	154	49, 49	60/250	NGC 1052	RLSy2	0.0050	399		40
3C 390.3	BLRG/Sy1		0.0561	577	158, 184	60/250	NGC 1068	Sy2/C-thick	0.0038	54		30
4U 0241+61	Sy1		0.0440	152	50, 49	60/250	NGC 2110	Sy2/C-thick	0.0076	194	58 58	60/250
Ark 120	Sy1		0.0327	277		50	NGC 2992	Sy2	0.0077	70		60
Ark 564	NLSy1		0.0247	447		20	NGC 4258	Sy2/LINER	0.0015	1463		40
Fairall 9	Sy1		0.0470	647		50	NGC 4388	Sy2/C-thick	0.0084	98.4		40
IC 4329A	Sy1	(1)	0.0161	573	148, 177	60/100	NGC 4507	Sy2	0.0118	145	46, 46	60/250
IRAS 13349+2438	Sy1/NLSy1	(2)	0.1076	45		50	NGC 4945	Sy2/C-thick	0.0019	998	208, 306	60/250
MCG-2-58-22	Sy1		0.0469	223	68, 68	50/250	NGC 5506	Sy2	0.0062	697	202, 200	60/250
MCG-6-30-15	NLSy1	(1)	0.0077	1965	505, 555	60/250	NGC 6240	Sy2/C-thick	0.0245	113		55
MCG+8-11-11	Sy1		0.0205	2		60	NGC 6300	Sy2	0.0037	27		40
Mkn 79	Sy1		0.0222	1292		30	NGC 7172	Sy2	0.0087	87	26, 26	50/250
Mkn 110	NLSy1		0.0353	1283		60	NGC 7314	Sy2	0.0048	252	73, 73	60/250
Mkn 279	Sy1		0.0305	180		40	NGC 7582	Sy2/C-thick	0.0053	185	43, 44	60/250
Mkn 335	NLSy1		0.0258	161		25	1ES 0229+200	BLLAC	0.1400	279		25
Mkn 509	Sy1		0.0344	738	197, 224	60/250	1ES 0414+009	BLLAC	0.2870	31		20
Mkn 590	Sy1		0.0264	32		40	1ES 0647+250	BLLAC	0.2030	42		20
Mkn 766	NLSy1	(1)	0.0129	771		25	1ES 1101-232	BLLAC	0.1860	194	29, 29	30/250
MR 2251-178	Sy1/QSO		0.0640	597	57, 144	50/250	1ES 1218+304	BLLAC	0.1836	10		20
NGC 3227	Sy1	(3)	0.0039	1050	303, 304	60/250	1ES 1727+502	BLLAC	0.0554	20		20
NGC 3516	Sy1	(4)	0.0088	1036	291, 290	60/250	1ES 1741+196	BLLAC	0.0840	11		20
NGC 3783	Sy1	(5)	0.0097	1563	204, 393	40/80	1ES 1959+650	BLLAC	0.0470	229	64, 64	50/250
NGC 3998	Sy1		0.0035	328		15	1ES 2344+514	BLLAC	0.0440	112		40
NGC 4051	NLSy1	(1)	0.0023	1972		40	1H 0323+342	FSRQ	0.0610	105		25
NGC 4151	Sy1		0.0033	562	179, 179	60/250	3C 273	FSRQ	0.1583	2378	429, 616	60/250
NGC 4593	Sy1	(6)	0.0090	1389	167, 326	60/250	3C 279	FSRQ	0.5362	2222	451, 635	25/250
NGC 5548	Sy1	(7)	0.0172	1012	294, 312	50/250	3C 454.3	FSRQ	0.8590	54	13, 13	40/250
NGC 7213	Sy1/Radio		0.0058	692		25	3C 66A	BLLAC	0.4440	162		20
NGC 7469	Sy1		0.0163	1097	243, 312	20/250	4C 29.45	FSRQ	0.7245	159		20
PDS 456	Sy1/QSO		0.1840	361		40	4C 71.07	FSRQ	2.1720	269	0, 39	25/250
PG 0052+251	Sy1		0.1545	170		40	BL Lac	BLLAC	0.0686	2311		30
PG 0804+761	Sy1	(8)	0.1000	382		50	CTA 102	FSRQ	1.0370	66		50
PG 1202+281	Sy1		0.1653	27		25	H 1426+428	BLLAC	0.1291	468		40
PG 1211+143	NLSy1		0.0809	131		40	Mkn 180	BLLAC	0.0453	15		20
Pictor A	Sy1/LINER		0.0351	34		40	Mkn 421	BLLAC	0.0300	2230	475, 481	30/250
PKS 0558-504	NLSy1		0.1370	932		20	Mkn 501	BLLAC	0.0336	728	153, 171	60/250
PKS 0921-213	FSRQ/Sy1		0.0520	92		40	NRAO 530	FSRQ	0.9020	136		20
TONS180	NLSy1		0.0620	326		25	PG 1553+113	FSRQ	0.3600	119		50
Cen A	NLRG		0.0018	913	109, 197	60/250	PKS 0528+134	FSRQ	2.0600	247		50
Circinus	Sy2/C-thick		0.0014	103	33, 32	60/250	PKS 0548-322	BLLAC	0.0690	13		40
Cygnus A	Sy2/Radio		0.0561	72		40	PKS 0829+046	FSRQ	0.1737	240		40
ESO 103-G35	Sy2		0.0133	163	50, 49	60/250	PKS 1510-089	FSRQ	0.3600	2091	260, 387	60/250
IC 5063	Sy2		0.0113	69		35	PKS 1622-297	FSRQ	0.8150	123		50
IRAS 04575-7537	Sy2		0.0181	49		50	PKS 2005-489	BLLAC	0.0710	400	96, 105	50/250
IRAS 18325-5926	Sy2		0.0202	332		40	PKS 2126-158	FSRQ	3.2680	34		20
MCG-2-40-4	Sy2		0.0252	3		25	PKS 2155-304	BLLAC	0.1160	902		40
MCG-5-23-16	Sy2/NELG		0.0085	180	55, 54	60/250	RGB J0710+591	BLLAC	0.1250	16		25
Mkn 3	Sy2		0.0135	54	15, 15	60/250	S5 0716+714	BLLAC	0.3000	656		15

NOTE. — Characteristics of our sample. Sources are listed alphabetically within three groups: Seyfert 1's, Seyfert 2's, and Blazars. "BLRG," "NLRG," or "Radio" indicates a radio loud non-blazar. "C-thick" indicates a known Compton-thick object. "NELG" indicates a Narrow Emission Line Galaxy. Source types were taken from NED. References for warm absorber parameters are (1) McKernan et al. (2007), (2) Blustin et al. (2005), (3) Markowitz et al. (2009), Turner et al. (2008), (5) Netzer et al. (2003), (6) Steenbrugge et al. (2003), (7) Steenbrugge et al. (2005) and (8) Pounds et al. (2003). HEXTE-A and B exposure times are given only for objects where those data were included in our spectral analysis.  $E_{\max}$  is the approximate maximum energy used in our spectral analysis for the PCA/HEXTE. For HEXTE, the whole energy range (20–250 keV) was used whenever the data were included, though in many cases it did not help to constrain the model fitting past  $\sim 50$ –100 keV. There were two exceptions which had significant background features around 100 keV that affected fitting and so were only included to 80–90 keV.

and 2 prior to 1998 December 23; PCU's 0 and 2 from 1998 December 23 until 2000 May 12; and PCU 2 only after 2000 May 12; using only events from the top Xe layer in order to maximize signal-to-noise. Standard screening was applied with time since SAA passage  $>20$  minutes and appropriate background models based on brightness were selected for each observation provided by the instrument team. Systematics up to 0.5% were included for objects with very long exposure times in order to try to get reduced  $\chi^2$  values between

1 and 2 in the best-fit model.

We also obtained HEXTE cluster A and B data for every object, though in many cases there was not sufficient detection to merit analysis of the HEXTE spectrum (see above). We did not combine HEXTE A and B data, and no HEXTE A data were used from after 2006 March when the cluster lost rocking (and therefore background gathering) capability. Background subtraction was performed separately for 16 s and 32 s rocking modes to eliminate problems with differences in the

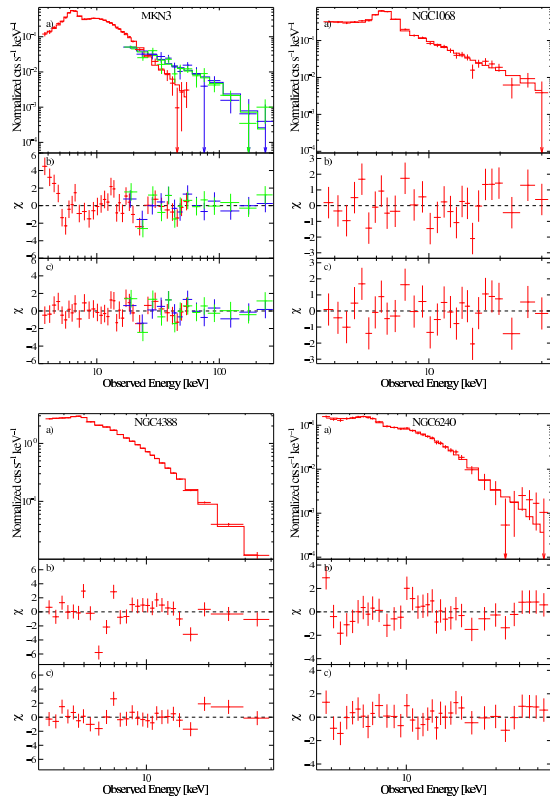


FIG. 2. — Data and data–model fit residuals for four of the complex sources (the other three can be found in RMR2011). Panel (a) shows the data and best fit model, (b) shows the fit residuals to the base model from Table 3, and (c) shows the fit residuals to the complex model found in Table 4. Note that for NGC 1068 we adopt the base model rather than the complex absorption model based on previous analyses of this source.

ratio of the on-source and off-source times (see RMR2011 for details). Standard HEXTE response matrices were used in all cases.

### 3. METHODS AND ANALYSIS

All spectral fitting for this analysis was done using XSPEC version 12.5.1k with cross-sections from Verner et al. (1996) and solar abundances from Wilms et al. (2000). We adopt a standard cosmology of  $H_0 = 73.0$ ,  $\Omega_\Lambda = 0.73$ , and  $\Omega_{\text{matter}} = 0.27$ . Uncertainties were calculated at the 90% confidence level ( $\Delta\chi^2 = 2.71$  for one interesting parameter) unless otherwise stated.

In our model fitting we included free renormalization constants for HEXTE-A and B with respect to the PCA. This accounts for cross-instrument calibration as well as differences in observing epochs for the different instruments. Additionally we included the RECORN component in all our models which renormalizes the background level to account for slight imperfections in background estimation. The adjustment was usually less than  $\sim 2\%$  percent. Bandpasses used for each object were determined on an ad hoc basis, excluding data above a certain energy if the background dominated the signal. For most objects the range used was 3.5–50 keV, though some of the very faint or very steep objects (NLSy1’s for example) only had usable data up to  $\sim 20$ –30 keV and some of the objects had high quality HEXTE data up to 100 keV and higher (RMR2011).

For all Seyferts our most basic model included an absorbed

power law continuum plus Fe  $K\alpha$  emission modeled by a simple Gaussian and the Compton reflection hump modeled with a disk geometry by PEXRAV (Magdziarz & Zdziarski 1995) which assumes a lamppost-like source above a near-infinite plane. Normalization and photon index of the incident power law in the PEXRAV model were tied to those of the continuum power law, abundances were set to solar, and the inclination angle ( $\cos i$ ) was frozen at 0.866 ( $30^\circ$ ), leaving only the reflection fraction  $R$  as a free parameter. See the discussion section for details on this model, its implications, and drawbacks. Galactic absorption was included for all sources (Kalberla et al. 2005) using the PHABS model in XSPEC. Warm absorbers were included where well-determined values were found in the literature and had the potential to affect the spectrum curvature above 3 keV (i.e., greater than 3% deviation in the spectrum), using an XSTAR table component, keeping the parameters frozen at the column density and ionization specified in the literature (see Table 1). Given the energy range and resolution of the PCA, our data were not sensitive to discrete lines from ionized absorption, however rollover from strong, mildly ionized absorbers could be detected below  $\sim 5$  keV. Additional cold absorption in the line of sight was included for many Seyfert 2’s, however for most Seyfert 1’s and some Seyfert 2’s cold absorption in addition to the Galactic column did not cause a significant change in  $\chi^2$  and was not included in the base model. Our best fit values for  $\Gamma$ ,  $N_{\text{H}}$  (the column density of cold material in addition to the Galactic column),  $R$ , and the Fe line equivalent width ( $EW$ ) are given in Tables 2 and 3 for Seyfert 1’s and 2’s respectively. A subsample of spectra are shown in Figure 1 to give an idea of the range of data quality in the sample.

The distribution of reduced  $\chi^2$  values is fairly smooth with an average value of  $\sim 1$ . From the average number of degrees of freedom in our sources we would expect a spread of roughly 0.25; instead we find a spread of almost twice that (the standard deviation is 0.46). At the high end this is likely due to systematic errors in very long observations. At the low end, there is a known issue with the data reduction software’s estimation of background errors. The software models the background counts spectrum based on multiple, long blank-sky observations, and then assumes Poissonian errors for the background counts spectrum appropriate for the exposure time of the observation of the target. However, the unmodeled residuals in the background are on the order of 1–2% (Jahoda et al. 2006). For sources with a total exposure less than  $\sim 10$ –30 ks, the Poissonian errors may be e.g., 2–4% of the counts, an overestimate of the true background errors, and this can in turn yield final errors on the net (background-subtracted) spectrum which are overestimates (Nandra et al. 2000). This explains why many of the sources with relatively short exposures have best-fit models with values of  $\chi_r^2$  near 0.6–0.7 (and in these cases, assumption of 1.5% background errors would yield net spectrum errors that are smaller by  $\sim 5$ –15%, yielding values of  $\chi_r^2 \sim 10$ –30% higher). We note that in these cases, because the errors are overestimates, our estimates of the errors on best-fit model parameters reported in the Tables are conservative. Additionally, for very faint sources ( $F_{2-10} \sim 4$ – $9 \times 10^{-12}$  erg  $\text{cm}^{-2} \text{s}^{-2}$ ) the average uncertainty in counts/channel could be as high as  $\sim 10$ –20%, even when exposure times were over 30 ks (e.g., IRAS 13349+2438, PG 1211+143, PKS 0921–213, NRAO 530, and PKS 0528+134), yielding similarly low values of  $\chi_{\text{red}}^2$ .

TABLE 2  
SEYFERT 1'S: BASE MODEL FIT PARAMETERS

Source Name	Flux <sub>2-10</sub> <sup>A</sup>	Log(L <sub>2-10</sub> )	$\Gamma$	$N_{\text{H}}$ ( $10^{22}\text{cm}^{-2}$ )	EW <sub>Fe</sub> (eV)	I <sub>Fe</sub> <sup>B</sup>	$R$	$FR$	$\chi^2/\text{dof}$
3C 111	49.1 ± 0.4	42.90	1.75 ± 0.02		90 ± 20	5.1 ± 1.0	≤ 0.1	≤ 0.1	39/50
3C 120	37.9 ± 0.7	43.45	1.88 ± 0.03		190 ± 70	8.0 ± 3.0	0.17 ± 0.07	0.2 ± 0.1	42/50
3C 382	44.4 ± 0.4	44.00	1.86 ± 0.04		105 ± 50	5.5 ± 2.6	0.13 ± 0.10	0.1 ± 0.1	26/54
3C 390.3	29.4 ± 0.2	43.80	1.76 ± 0.04		100 ± 70	3.6 ± 2.4	0.2 ± 0.1	0.2 ± 0.1	31/54
4U 0241+61	34.5 ± 0.2	43.65	1.74 ± 0.04		200 ± 40	8.0 ± 1.4	0.3 ± 0.1	0.3 ± 0.2	67/54
Ark 120	34.5 ± 0.3	43.40	2.07 ± 0.05		240 ± 40	8.4 ± 1.4	0.5 ± 0.2	0.5 ± 0.2	17/29
Ark 564	18.5 ± 0.3	42.88	2.69 ± 0.04		220 ± 120	3.2 ± 1.7	-	-	22/20
Fairall 9	17.7 ± 0.2	43.42	2.00 ± 0.07		180 ± 50	3.4 ± 1.0	0.5 ± 0.3	0.4 ± 0.3	27/23
IC 4329A	102.6 ± 0.4	43.25	1.95 ± 0.02	*	100 ± 20	11.2 ± 2.1	0.4 ± 0.1	0.3 ± 0.1	69/48
IRAS 13349+2438	4.0 ± 0.2	43.51	2.27 ± 0.19	*	460 ± 460	2.0 ± 2.0	-	-	14/27
MCG-2-58-22	25.7 ± 0.2	43.58	1.70 ± 0.04		160 ± 30	4.9 ± 1.0	≤ 0.2	≤ 0.2	47/54
MCG-6-30-15	41.6 ± 0.3	42.22	2.25 ± 0.05	*	190 ± 40	8.7 ± 2.0	1.5 ± 0.3	1.2 ± 0.3	45/54
MCG+8-11-11	53.8 ± 0.9	43.19	1.70 ± 0.07		210 ± 60	11.9 ± 3.2	≤ 0.3	≤ 0.3	15/27
Mkn 79	20.3 ± 0.2	42.83	1.90 ± 0.07		200 ± 40	4.4 ± 0.9	0.7 ± 0.3	0.6 ± 0.3	26/28
Mkn 110	30.9 ± 0.2	43.41	1.80 ± 0.04		65 ± 20	2.1 ± 0.6	0.14 ± 0.11	0.1 ± 0.1	34/28
Mkn 279	19.2 ± 0.3	43.08	1.89 ± 0.07		170 ± 60	3.7 ± 1.2	≤ 0.5	≤ 0.4	22/22
Mkn 335	10.7 ± 0.2	42.68	2.11 ± 0.06		190 ± 70	2.0 ± 0.7	-	-	37/21
Mkn 509	39.5 ± 0.2	43.50	1.87 ± 0.03		80 ± 20	3.6 ± 1.1	0.2 ± 0.1	0.2 ± 0.1	46/54
Mkn 590	33.4 ± 0.5	43.20	1.75 ± 0.08		130 ± 70	4.9 ± 2.4	≤ 0.5	≤ 0.5	17/27
Mkn 766	27.8 ± 0.1	42.51	2.33 ± 0.09	*	1900 ± 950	1.6 ± 0.8	0.9 ± 0.4	0.7 ± 0.3	26/20
MR 2251-178	39.1 ± 0.3	44.03	1.76 ± 0.01		60 ± 40	2.6 ± 1.7	≤ 0.03	≤ 0.03	42/53
NGC 3227	32.2 ± 0.2	41.52	1.80 ± 0.03	*	160 ± 30	5.8 ± 1.2	0.3 ± 0.1	0.3 ± 0.1	33/54
NGC 3516	36.2 ± 0.3	42.28	1.85 ± 0.04	*	160 ± 40	7.1 ± 2.0	0.8 ± 0.2	0.6 ± 0.1	43/53
NGC 3783	60.9 ± 1.0	42.59	1.89 ± 0.04	*	290 ± 80	20.0 ± 5.4	0.3 ± 0.1	0.3 ± 0.1	52/42
NGC 3998	7.7 ± 1.0	40.80	2.04 ± 0.27		≤ 390	≤ 15.8	≤ 1.1	≤ 0.9	18/14
NGC 4051	21.1 ± 1.8	40.88	2.30 ± 0.08	*	140 ± 40	2.9 ± 0.8	2.0 ± 0.8	1.6 ± 0.7	22/22
NGC 4151	164.4 ± 0.9	42.39	1.88 ± 0.01	21.2 ± 1.0	118 ± 88	39.6 ± 29.	1.3 ± 0.1	1.2 ± 0.1	100/61 <sup>C</sup>
NGC 4593	38.4 ± 0.3	42.32	1.85 ± 0.03	*	200 ± 30	8.2 ± 1.1	0.3 ± 0.1	0.3 ± 0.1	51/54
NGC 5548	41.1 ± 0.2	42.91	1.89 ± 0.02	*	105 ± 25	4.7 ± 1.1	0.3 ± 0.1	0.3 ± 0.1	46/54
NGC 7213	18.9 ± 0.7	41.65	1.91 ± 0.10		220 ± 45	4.1 ± 0.9	≤ 0.3	≤ 0.3	30/19
NGC 7469	27.1 ± 0.3	42.69	1.94 ± 0.05		140 ± 50	4.1 ± 1.4	0.6 ± 0.2	0.5 ± 0.2	47/44
PDS 456	7.0 ± 0.1	44.23	3.52 ± 0.10		580 ± 320	4.8 ± 2.7	-	-	24/22
PG 0052+251	7.3 ± 0.1	44.07	1.89 ± 0.17		≤ 590	≤ 5.8	≤ 1.4	≤ 1.3	16/22
PG 0804+761	11.2 ± 0.2	43.89	2.00 ± 0.06	*	120 ± 60	1.7 ± 0.8	≤ 0.3	≤ 0.2	21/23
PG 1202+281	5.9 ± 0.2	44.04	2.10 ± 0.14		200 ± 140	1.5 ± 1.1	-	-	8/21
PG 1211+143	5.5 ± 0.1	43.39	1.99 ± 0.08		190 ± 90	1.2 ± 0.6	-	-	14/28
Pictor A	19.8 ± 0.4	43.22	1.73 ± 0.05		110 ± 60	2.5 ± 1.3	≤ 0.2	≤ 0.2	14/26
PKS 0558-504	14.8 ± 0.2	44.27	2.20 ± 0.07		≤ 105	≤ 1.9	≤ 0.5	≤ 0.4	27/19
PKS 0921-213	7.8 ± 0.2	43.15	1.66 ± 0.14		≤ 190	≤ 1.7	≤ 0.8	≤ 0.8	8/29
TONS180	7.4 ± 0.1	43.29	2.43 ± 0.23		360 ± 300	2.2 ± 1.8	≤ 2.0	≤ 1.5	20/20

NOTE. — Best fit parameters for Seyfert 1's with the base model. Listed are the 2–10 keV observed flux, 2–10 keV unabsorbed luminosity, photon index, column density above the Galactic column, equivalent width of the Fe K $\alpha$  line, the reflection strength as determined by PEXRAV, the flux ratio of the reflection to the continuum in the 15–50 keV range, and  $\chi^2/\text{dof}$ . The “-” symbol indicates a parameter was unconstrained. The “\*” symbol indicates that a warm absorber was modeled with fixed parameters, see references in Table 1.

<sup>A</sup> Flux is in units of  $10^{-12}$  erg  $\text{cm}^{-2}$   $\text{s}^{-1}$ .

<sup>B</sup> Fe line intensity is in units of  $10^{-5}$  photons  $\text{cm}^{-2}$   $\text{s}^{-1}$ .

<sup>C</sup> Fit to complex model given in Table 4.

TABLE 3  
SEYFERT 2'S: BASE MODEL FIT PARAMETERS

Source Name	Flux <sub>2-10</sub> <sup>A</sup>	Log(L <sub>2-10</sub> )	$\Gamma$	$N_{\text{H}}$ (10 <sup>22</sup> cm <sup>-2</sup> )	EW <sub>Fe</sub> (eV)	$I_{\text{Fe}}$ <sup>B</sup>	$R$	$FR$	$\chi^2/\text{dof}$
Cen A	280.7 ± 5.5	42.05	1.84 ± 0.01	16.2 ± 0.3	95 ± 10	50.7 ± 5.9	≤ 0.01	≤ 0.04	134/52
Circinus	22.9 ± 0.8	40.66	1.57 ± 0.03		1520 ± 30	39.0 ± 0.9	6.5 ± 0.6	6.8 ± 0.7	786/53 <sup>C</sup>
Cygnus A	78.7 ± 8.9	44.36	2.06 ± 0.09	7.1 ± 2.7	370 ± 70	42.1 ± 7.7	≤ 0.1	≤ 0.1	20/20
ESO 103-G35	22.0 ± 0.3	42.74	1.83 ± 0.10	28.3 ± 2.1	290 ± 70	15.8 ± 4.1	0.5 ± 0.2	0.5 ± 0.2	44/53
IC 5063	12.2 ± 0.2	42.37	1.65 ± 0.36	31.7 ± 11.3	180 ± 120	5.8 ± 3.8	≤ 1.0	≤ 1.0	18/19
IRAS 04575-7537	21.7 ± 1.4	42.72	2.48 ± 0.22	3.6 ± 2.6	≤ 350	4.2 ± 4.7	1.5 <sup>+2.9</sup> <sub>-0.9</sub>	1.1 <sup>+2.0</sup> <sub>-0.6</sub>	10/25
IRAS 18325-5926	21.5 ± 0.2	42.78	2.71 ± 0.23		820 ± 270	14.3 ± 4.6	4.5 ± 3.3	3.1 ± 2.3	20/20
MCG-2-40-4	17.6 ± 0.7	42.86	1.69 ± 0.15		340 ± 220	6.3 ± 4.1	≤ 0.8	≤ 0.8	16/28
MCG-5-23-16	89.4 ± 1.3	42.71	1.85 ± 0.04	3.7 ± 0.8	140 ± 20	16.0 ± 2.8	0.3 ± 0.1	0.3 ± 0.1	40/52
Mkn 3	7.0 ± 1.6	42.75	1.43 ± 0.15	90.6 ± 7.3	230 ± 70	9.2 ± 2.9	0.4 ± 0.3	0.5 ± 0.4	100/53 <sup>C</sup>
Mkn 348	11.6 ± 0.2	42.46	1.51 ± 0.09	17.3 ± 2.1	125 ± 45	3.1 ± 1.1	0.3 ± 0.2	0.4 ± 0.2	45/53
NGC 526A	39.5 ± 1.0	43.07	1.80 ± 0.08	4.6 ± 1.6	90 ± 40	4.5 ± 2.3	0.4 ± 0.2	0.3 ± 0.2	47/53
NGC 1052	5.9 ± 0.1	41.18	1.71 ± 0.29	13.6 ± 5.2	190 ± 90	2.0 ± 1.0	≤ 1.6	≤ 1.6	41/24
NGC 1068	7.6 ± 5.6	41.28	1.60 ± 0.22		1880 ± 130	16.8 ± 1.1	≤ 2.0	≤ 2.1	27/21 <sup>C</sup>
NGC 2110	37.5 ± 0.6	42.28	1.73 ± 0.06	6.0 ± 1.2	190 ± 40	9.6 ± 2.2	≤ 0.2	≤ 0.2	30/53
NGC 2992	22.3 ± 2.0	41.97	1.78 ± 0.18		290 ± 90	7.4 ± 2.4	≤ 0.8	≤ 0.7	12/27
NGC 4258	7.7 ± 1.5	40.23	1.80 ± 0.10	8.4 ± 2.0	≤ 250	≤ 3.0	≤ 0.4	≤ 0.4	23/28
NGC 4388	45.2 ± 1.8	42.56	1.09 ± 0.08		270 ± 30	15.9 ± 1.8	≤ 0.1	≤ 0.1	79/20 <sup>C</sup>
NGC 4507	14.0 ± 3.0	42.83	1.77 ± 0.07	86.8 ± 2.9	150 ± 30	11.9 ± 2.5	0.3 ± 0.1	0.3 ± 0.1	78/52
NGC 4945	4.4 ± 0.2	40.97	1.16 ± 0.02		570 ± 85	3.5 ± 0.5	19 ± 2	17 ± 5	1488/53 <sup>C</sup>
NGC 5506	86.4 ± 0.4	42.35	1.98 ± 0.03		320 ± 50	34.5 ± 5.2	0.8 ± 0.1	0.7 ± 0.1	84/53
NGC 6240	4.1 ± 2.1	42.92	1.45 ± 0.18		≤ 140	≤ 0.8	10 <sup>+12</sup> <sub>-4</sub>	10 <sup>+11</sup> <sub>-4</sub>	36/27 <sup>C</sup>
NGC 6300	6.2 ± 0.1	40.87	1.32 ± 0.46	14.9 ± 7.6	450 ± 120	5.1 ± 1.4	≤ 4.3	≤ 4.2	10/21
NGC 7172	15.9 ± 0.6	42.13	1.66 ± 0.16	16.2 ± 3.4	180 ± 110	5.7 ± 3.5	≤ 0.4	≤ 0.4	61/53
NGC 7314	34.6 ± 2.1	41.72	1.99 ± 0.10		200 ± 80	7.5 ± 3.0	0.6 ± 0.2	0.6 ± 0.2	39/53
NGC 7582	10.5 ± 5.4	41.51	1.70 ± 0.10	13.3 ± 2.6	340 ± 70	6.7 ± 1.4	2.7 ± 0.9	2.7 ± 0.7	38/53 <sup>C</sup>

NOTE. — Best fit parameters for Seyfert 2's with the base model. Listed are the 2–10 keV observed flux, 2–10 keV unabsorbed luminosity, photon index, column density above the Galactic column, equivalent width of the Fe K $\alpha$  line, the reflection strength as determined by PEXRAV, the flux ratio of the reflection to the continuum in the 15–50 keV range, and  $\chi^2/\text{dof}$ . The “-” symbol indicates a parameter was unconstrained.

<sup>A</sup> Flux is in units of 10<sup>-12</sup> erg cm<sup>-2</sup> s<sup>-1</sup>.

<sup>B</sup> Fe line intensity is in units of 10<sup>-5</sup> photons cm<sup>-2</sup> s<sup>-1</sup>

<sup>C</sup> Fit to complex model given in Table 4. Note that we have adopted the fit given in this table for NGC 1068 (see Appendix B for details).



TABLE 4  
 COMPLEX MODELS FOR SEYFERTS

Source Name	Flux <sub>2–10</sub> <sup>A</sup>	$\Gamma_{\text{hard}}$	$\Gamma_{\text{soft}}$	$A_{\text{soft}}/A_{\text{hard}}^{\text{B}}$	Soft $N_{\text{H}}$ ( $10^{22}\text{cm}^{-2}$ )	Hard $N_{\text{H}}$ ( $10^{22}\text{cm}^{-2}$ )	EW <sub>Fe</sub> (eV)	$I_{\text{Fe}}^{\text{C}}$	$R$	$E_{\text{roll}}$	$\chi^2/\text{dof}$
NGC 4151	$175 \pm 24$	$1.90 \pm 0.02$	*	$0.44 \pm 0.20$	$\leq 13.6$	$50_{-10}^{+50}$	$299_{-139}^{+251}$	$109 \pm 71$	$1.0 \pm 0.2$		67/60
Circinus	$23.2 \pm 2.7$	$1.2 \pm 0.2$	$2.5 \pm 0.4$	$1.1 \pm 0.3$		$920_{-150}^{+120}$	$2400 \pm 100$	$52 \pm 1$	$1.1 \pm 0.3$	$41_{-10}^{+6}$	44/50
Mkn 3	$7.6 \pm 1.7$	$1.44 \pm 0.10$	*	$0.05 \pm 0.01$		$130_{-12}^{+4}$	$564_{-141}^{+141}$	$17.6 \pm 4.4$	$\leq 0.19$		44/52
NGC 1068	$7.6 \pm 5.6$	$1.53 \pm 0.14$	*	$0.3 \pm 0.3$		$\geq 780$	$\leq 4302$	$57_{-33}^{+160}$	$\leq 1$		22/20
NGC 4388	$48 \pm 17$	$1.40 \pm 0.13$	*	$0.5 \pm 0.1$		$92_{-21}^{+8}$	$257_{-67}^{+37}$	$22.8 \pm 4.6$	$\leq 0.20$		25/19
NGC 4945	$5.1 \pm 1.2$	$0.88 \pm 0.12$	$2.06_{-0.1}^{+0.6}$	$0.8 \pm 0.1$		$425 \pm 25$	$1420 \pm 120$	$6.0 \pm 0.5$	$\leq 0.1$	$59 \pm 7$	39/51
NGC 6240	$4.3 \pm 2.2$	$1.65 \pm 0.45$	*	$0.17_{-0.04}^{+0.13}$		$200_{-80}^{+10}$	$139_{-139}^{+32}$	$5.9 \pm 3.6$	$\leq 2.90$		22/28
NGC 7582	$10 \pm 6$	$1.75 \pm 0.12$	*	$0.69 \pm 0.15$	$16.5 \pm 3.9$	$230_{-120}^{+150}$	$324_{-89}^{+74}$	$9.4 \pm 2.4$	$1.3_{-0.4}^{+0.6}$		38/51

NOTE. — Best fit parameters for Seyferts requiring complex modeling. For all sources the ratio of the soft to hard power law components are given. This may indicate partial covering absorption, scattered emission, or contamination from extended emission in the host galaxy. The hard power law is assumed to be entirely due to AGN activity.  $\Gamma_{\text{soft}}$  was tied to  $\Gamma_{\text{hard}}$  (indicated by the "\*" symbol) unless it was a significant improvement to leave it free (this was the case in only one source, NGC 4945, which has significant starburst activity in the host galaxy). NGC 4945 and Circinus also required high energy rollovers modeled by CUTOFFPL with a rollover energy,  $E_{\text{roll}}$ , defined as the energy at which the continuum is  $1/e$  times the initial value.

<sup>A</sup> Flux is in units of  $10^{-12}$  erg  $\text{cm}^{-2}$   $\text{s}^{-1}$ .

<sup>B</sup> The ratio of the normalization at 1 keV of the soft power law to that of the hard power law.

<sup>C</sup> Fe line intensity is in units of  $10^{-5}$  photons  $\text{cm}^{-2}$   $\text{s}^{-1}$ .

In a few cases more complex models were required, specifically either partial covering absorption or scattered nuclear emission were necessary in a handful of sources. Best fit parameters for these models are shown in Table 4 and spectra for those sources not included in RMR2011 are shown in Figure 2. The majority of these sources are Compton-thick Seyfert 2's, with the exception of NGC 4151. Details on these sources can be found in Appendix B. Note for many of these Compton-thick sources it can be difficult to accurately constrain the parameters of the coronal power-law component, since there can be degeneracy between  $\Gamma$  and the parameters of the CRH and the absorber (see, e.g., RMR2011). An additional complication is the presence of excess soft emission (below  $\sim 10$  keV), usually modeled as a power law. This "contaminating" emission can arise from nuclear emission scattered in a diffuse, extended plasma, unresolved point sources in the host galaxy, starburst activity in the host galaxy, or any combination of these.

Our basic model for the blazars in our sample was a simple power law. The best fit values for  $\Gamma$  and the power law normalization are listed in Table 5. We also tried a broken power law model for all blazars but it was only a significant improvement in fit for four objects, 1ES 1101–232, 1ES 1959+650, Mkn 421 and Mkn 501. Best fit parameters for the broken power law model for these objects are given in Table 6.

#### 4. DISCUSSION

Our excavation of the *RXTE* archive has produced a unique sample of 100 AGNs with spectral data from 3.5 keV to  $\gtrsim 20$  keV. The breadth of this energy range has allowed us to explore key spectral components that have not been well-studied to date. Most significantly, quantifying the Compton reflection hump requires spectral sensitivity over a broad energy range which many other modern X-ray observatories lack (*Chandra*, *XMM-Newton*, *Swift*). *RXTE*'s ability to observe the very hard X-ray properties of AGNs simultaneously with their mid-range (2–10 keV) X-ray properties eliminates problems associated with non-simultaneous observing which can be particularly severe in highly variable objects. Additionally,

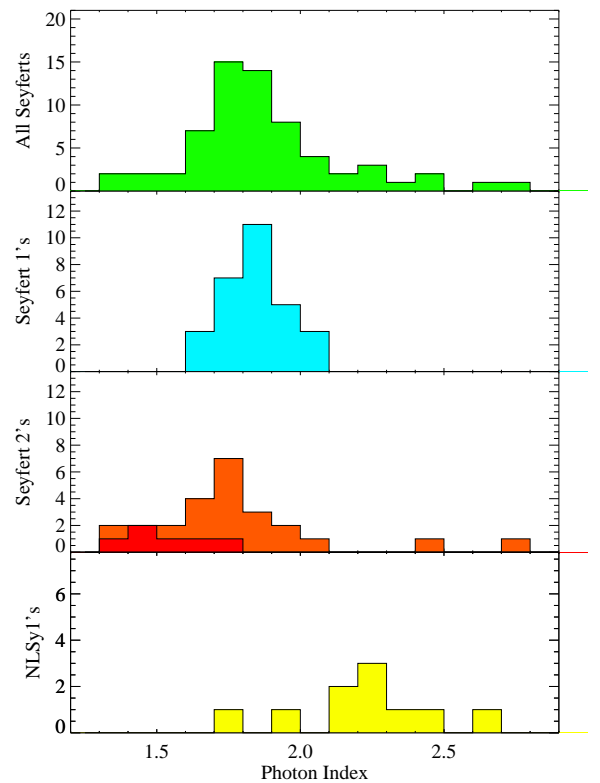


FIG. 3.—  $\Gamma$  distribution by type. Seyfert 2's are divided into Compton-thin (orange) and Compton-thick (red). Typical Seyfert 1's and Seyfert 2's are all consistent with an average photon index of 1.8–1.9 as has been found in previous works. NLSy1's show much steeper X-ray spectra with  $\Gamma > 2$  in most sources. Note that two Seyfert 2's, IRAS 18325–5926 and IRAS 04575–7537 have X-ray characteristics similar to NLSy1's, being very steep without absorption  $\geq 10^{22}$   $\text{cm}^{-2}$  and a poorly constrained CRH. NGC 4945 is an extreme outlier and is not shown on this plot.

*RXTE* does not suffer from cross-calibration uncertainties between instruments such as between the *Suzaku* XIS and HXD or between the *BeppoSAX* MECS and PDS instruments. Sev-

TABLE 5  
BLAZARS: POWER-LAW MODEL PARAMETERS

Source Name	Flux <sub>2-10</sub> <sup>A</sup>	Log(L <sub>2-10</sub> )	Γ	A (10 <sup>-2</sup> )	χ <sup>2</sup> /dof
1ES 0229+200	15.1 ± 0.8	44.69	1.88 ± 0.03	0.49 ± 0.02	37/25
1ES 0414+009	8.8 ± 1.9	43.82	2.68 ± 0.12	0.90 ± 0.19	14/22
1ES 0647+250	17.8 ± 2.4	45.03	2.67 ± 0.08	1.79 ± 0.25	19/21
1ES 1101-232	40.7 ± 1.3	44.43	2.51 ± 0.02	3.29 ± 0.10	74/54 <sup>B</sup>
1ES 1218+304	12.1 <sup>+2</sup> <sub>-6</sub>	43.29	2.53 ± 0.20	1.01 <sup>+0.17</sup> <sub>-0.47</sub>	8/16
1ES 1727+502	9.5 ± 1.4	44.30	2.00 ± 0.07	0.37 ± 0.05	11/23
1ES 1741+196	19.1 ± 3.3	44.69	2.15 ± 0.10	0.93 ± 0.16	6/17
1ES 1959+650	148.3 ± 1.9	44.97	2.12 ± 0.01	6.83 ± 0.09	71/59 <sup>B</sup>
1ES 2344+514	25.0 ± 1.2	43.95	2.15 ± 0.03	1.21 ± 0.06	30/28
1H 0323+342	15.3 ± 1.2	44.34	1.88 ± 0.04	0.50 ± 0.04	28/24
3C 273	98.5 ± 1.0	43.51	1.70 ± 0.00	2.43 ± 0.02	72/60
3C 279	9.1 ± 0.5	43.58	1.68 ± 0.03	0.22 ± 0.01	88/51
3C 454.3	66.7 ± 3.1	45.22	1.63 ± 0.02	1.47 ± 0.07	28/53
3C 66A	6.4 ± 1.0	45.24	2.73 ± 0.10	0.70 ± 0.11	14/15
4C 29.45	3.1 ± 0.5	46.52	1.74 ± 0.08	0.08 ± 0.01	27/24
4C 71.07	16.0 ± 7.7	44.93	1.53 ± 0.02	0.30 ± 0.14	45/37
BL Lac	11.2 ± 0.5	46.70	1.83 ± 0.02	0.34 ± 0.02	36/26
CTA 102	9.7 ± 1.3	43.55	1.81 ± 0.07	0.28 ± 0.04	30/28
H 1426+428	23.6 ± 0.7	45.84	1.92 ± 0.02	0.81 ± 0.02	18/28
Mkn 180	12.3 ± 2.7	44.42	2.70 ± 0.13	1.28 ± 0.28	8/14
Mkn 421	419.4 ± 5.6	43.23	2.70 ± 0.01	43.86 ± 0.58	283/57 <sup>B</sup>
Mkn 501	109.6 ± 1.1	44.40	2.00 ± 0.01	4.26 ± 0.04	76/59 <sup>B</sup>
NRAO 530	3.5 ± 1.0	43.92	2.24 ± 0.16	0.19 ± 0.05	12/15
PG 1553+113	14.5 ± 1.2	45.27	2.61 ± 0.05	1.36 ± 0.11	18/28
PKS 0528+134	4.1 ± 0.5	45.10	1.65 ± 0.06	0.09 ± 0.01	21/28
PKS 0548-322	32.9 ± 3.0	46.06	2.15 ± 0.05	1.59 ± 0.15	12/28
PKS 0829+046	3.3 ± 0.8	44.02	2.11 ± 0.14	0.15 ± 0.03	22/17
PKS 1510-089	6.7 ± 0.4	44.76	1.35 ± 0.03	0.09 ± 0.01	111/59
PKS 1622-297	8.4 ± 0.6	45.57	2.07 ± 0.04	0.36 ± 0.03	29/28
PKS 2005-489	56.0 ± 0.9	44.27	2.46 ± 0.01	4.25 ± 0.07	40/54
PKS 2126-158	8.4 ± 1.0	46.78	1.66 ± 0.07	0.19 ± 0.02	12/25
PKS 2155-304	33.2 ± 0.6	44.47	2.68 ± 0.01	3.40 ± 0.07	24/19
RGB J0710+591	40.9 ± 3.4	44.63	2.18 ± 0.05	2.07 ± 0.17	13/24
S5 0716+714	3.9 ± 0.8	44.37	2.51 ± 0.11	0.32 ± 0.06	17/13

NOTE. — Best fit parameters for blazars with the simple power law model. Listed are the 2–10 keV flux, the photon index, and the normalization of the power law defined as ph keV<sup>-1</sup> cm<sup>-2</sup> s<sup>-1</sup> at 1 keV. Note that 1ES 1218+0304 includes additional systematic errors due to possible contamination by Mkn 766 as detailed in the text.

<sup>A</sup> Flux is in units of 10<sup>-12</sup> erg cm<sup>-2</sup> s<sup>-1</sup>.

<sup>B</sup> Better fit by broken power law model given in Table 6.

eral AGN studies at high X-ray energies ( $\gtrsim 10$  keV) have been performed with *BeppoSAX*, *CGRO-OSSE*, *Swift-BAT*, *INTEGRAL*, and *Suzaku* (Dadina 2007; Zdziarski et al. 2000; Tueller et al. 2010; Ricci et al. 2011; and Patrick et al. 2012, respectively), particularly focusing on Seyferts. We begin our discussion by presenting the results of our analysis and then comparing them to those from other surveys.

#### 4.1. Results for the Seyfert Sample

Making use of the large sample provided by the *RXTE* archive we can examine spectral properties of different types of AGNs. We have divided our sample into optically classified Seyfert 1's, Seyfert 2's, NLSy1's, Compton-thick Seyfert 2's and blazars (which will be discussed in a following sec-

tion). Unweighted average parameter values for the various Seyfert sub-types are given in Table 7. The distributions of  $\Gamma$  and  $R$  by object type are given in Figures 3 and 4.

The average photon index for our entire sample of Seyferts was 1.94. For Seyfert 1's and Compton-thin Seyfert 2's the average photon indices were 1.86 and 1.79 respectively with standard deviations of  $\sim 0.12$ . The similarity in  $\Gamma$  between these two classes of objects supports the Seyfert 1/2 unification schemes since we would expect the intrinsic photon indices to be unrelated to the viewing angle. They are also consistent with the values of  $\sim 1.8$ – $1.9$  generally accepted to be the average range of power law photon indices in Seyferts (e.g. Nandra & Pounds 1994, Gondek et al. 1996, Dadina 2008). The Compton-thick Seyfert 2's had an average photon



TABLE 6  
 BLAZARS: BROKEN POWER-LAW MODEL PARAMETERS

Source Name	Flux <sub>2-10</sub> <sup>A</sup>	Log(L <sub>2-10</sub> )	Γ <sub>1</sub>	Γ <sub>2</sub>	A (10 <sup>-2</sup> )	E <sub>break</sub> (keV)	χ <sup>2</sup> /dof
1ES 1101-232	39.3 ± 0.6	44.96	2.31 ± 0.20	2.56 ± 0.06	2.49 ± 0.63	4.6 ± 1.5	55/52
1ES 1959+650	145.4 ± 0.7	44.33	1.99 ± 0.07	2.14 ± 0.01	5.70 ± 0.52	4.9 ± 0.6	34/57
Mkn 421	367 ± 7	44.35	2.41 ± 0.09	2.75 ± 0.01	26.01 ± 3.81	6.6 ± 0.4	73/55
Mkn 501	109.0 ± 0.3	43.92	1.97 ± 0.02	2.02 ± 0.01	4.04 ± 0.11	6.9 ± 1.2	55/57

NOTE. — Best fit parameters for blazars with the broken power law model. The normalization,  $A$  is defined as  $\text{ph keV}^{-1} \text{cm}^{-2} \text{s}^{-1}$  at the break energy. All show significant improvement in the fit over a simple power law, though 1ES 1101-232 has a break energy very close to the edge of the bandpass and should be treated with caution.

<sup>A</sup> Flux is in units of  $10^{-12} \text{ erg cm}^{-2} \text{ s}^{-1}$ .

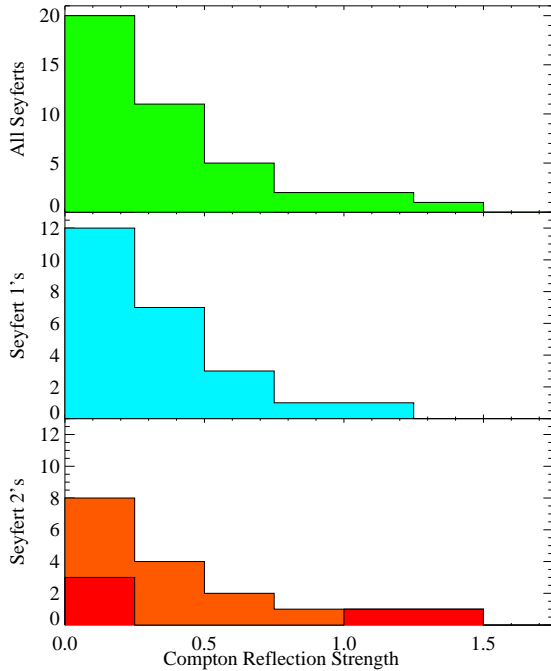


FIG. 4.—  $R$  distribution by type. Seyfert 2's are divided into Compton-thin (orange) and Compton-thick (red). NLSy1's are not included with the Seyfert 1's. Sources with only upper limits are all located in the far left bin and sources without well-determined  $R$  values (i.e., with  $\sigma_R/R > 1$  and upper limits  $\geq 0.5$ ) are left off this plot.

index of 1.77 with a standard deviation of 0.26, although for these sources it is very difficult to measure the intrinsic photon index accurately since the extreme curvature of the spectrum gives little leverage for measuring  $\Gamma$ .

NLSy1's had an average photon index of 2.24 (with a standard deviation of 0.24), significantly higher than other Seyferts and consistent with the idea that these objects are in a different regime of accretion (Pounds et al. 1995). If Seyfert 1's and 2's share a common central engine, we would expect to see Seyfert 2's with similar properties to NLSy1's which could not be identified optically (since the BLR is obscured in Seyfert 2's). IRAS 18325–5926 and IRAS 04575–7537 are Seyfert 2's which show very soft power laws with photon indices of  $2.71 \pm 0.23$  and  $2.48 \pm 0.22$ , respectively. These sources resemble NLSy1's in their X-ray spectra, and may be part of a class of objects that have been a missing piece in the Seyfert 1/2 unification puzzle. NGC 5506 has been shown to be a hidden NLSy1 (Nagar et al. 2002) and has a photon index of  $1.98 \pm 0.03$ .

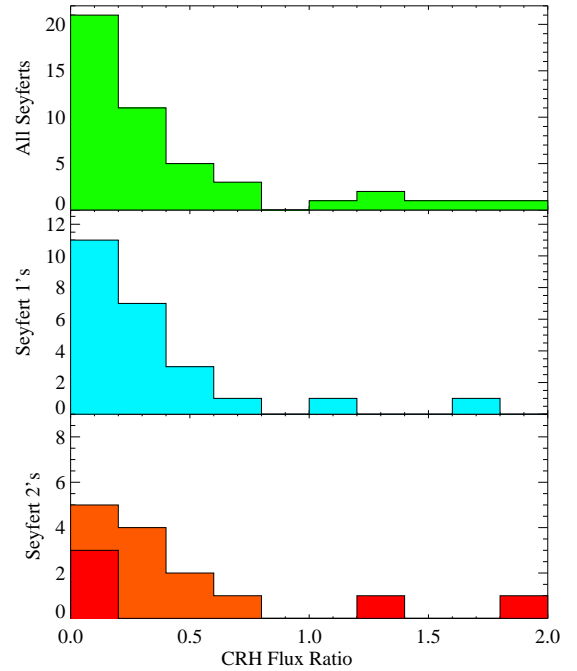


FIG. 5.—  $FR$  distribution by type, where  $FR$  is defined as the ratio of the CRH flux to the power law flux in the 15–50 keV range and can be used to make comparisons with other reflection models which are commonly utilized (i.e.,  $FR$  is model independent). Seyfert 2's are divided into Compton-thin (orange) and Compton-thick (red). NLSy1's are not included with the Seyfert 1's. Sources with only upper limits are located in the far left bin and sources without well-determined  $FR$  values (i.e., with  $\sigma_{FR}/FR > 1$  and upper limits  $\geq 0.5$ ) are left off this plot.

We detected a strong CRH ( $R \gtrsim 0.2$ ) significant at the  $5\sigma$  level in 28 of the 66 Seyferts in our sample. Only 5 showed no contribution from the CRH at all ( $R < 0.1$ ). Thus, of the 33 sources which had enough counts enough to measure  $R$  with high significance,  $\sim 85\%$  showed at least some contribution from the CRH. The remaining 33 Seyferts did not have well measured CRH's due to a lack of counts above 10 keV and/or a weak reflection hump. Averages were calculated excluding sources with poorly constrained  $R$  values, i.e., those with only upper limits that were greater than 0.5. The average reflection strength for all Seyferts was 0.45 with a standard deviation of 0.76 (note that the distribution is non-Gaussian and highly skewed; see Figure 4). Note also that in Compton-thick sources and NLSy1's it is difficult to constrain the level of the power law continuum against which  $R$  is measured. These sources are likely to have overestimated  $R$  values for this reason. Seyfert 1's had an average  $R$  value of 0.27 and

TABLE 7  
AVERAGE SPECTRAL PARAMETER  
VALUES BY OPTICAL CLASSIFICATION

Type	$\Gamma$	$R$
All Seyferts	1.90	0.45
Narrow Line Seyfert 1's	2.24	0.89
Seyfert 1's	1.86	0.27
Compton-thin Seyfert 2's	1.85	0.27
Compton-thick Seyfert 2's	1.40	0.48
Blazars	2.1	
BLLAC	2.3	
FSRQ	1.8	

NOTE. — Average model parameter values for sources in our sample by type. Objects with poorly constrained parameters have been omitted when calculating these averages. Note that the high average  $R$  value for all Seyferts is due in large part to the contribution from the steep NLSy1's. For typical Seyfert 1's and 2's the average  $R$  is  $\sim 0.3$ .

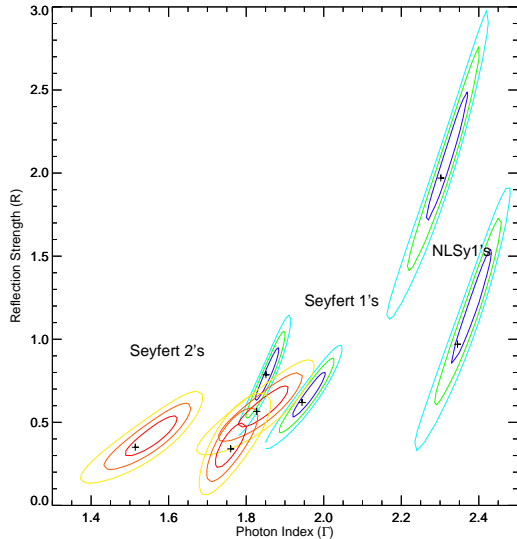


FIG. 6.— Contours for selected low flux ( $1-4 \times 10^{-11}$  erg  $\text{cm}^{-2}$   $\text{s}^{-1}$ ) Seyferts showing degeneracy between  $R$  and  $\Gamma$ . The contour lines going from dark to light (inner to outer) correspond to  $3\sigma$ ,  $2\sigma$ , and  $1\sigma$ ; blue is used for Seyfert 1's and red is used for Seyfert 2's. From left to right the sources are Mkn 348, NGC 4507, ESO 103-G35, NGC 3516, NGC 7469, NGC 4051, and Mkn 766.  $R$  is particularly difficult to constrain in NLSy1's compared to the other Seyfert classifications due to the steepness of the spectra.

Compton-thin Seyfert 2's had an average of 0.27, and standard deviations of 0.28 and 0.27 respectively, consistent with Seyfert 1's and 2's having on average the same amount of reflected flux. Contour plots of  $\Gamma$  versus  $R$  for selected Seyferts are shown in Figure 6.

We have also created stacked spectra for Seyfert 1's, Compton-thin Seyfert 2's and Narrow Line Seyfert 1's, including all objects weighted by exposure (excluding Cen A which dominates the Seyfert 2 stacked spectrum otherwise). Combining these into an overall X-ray SED with the correct relative abundances of different source types could give a good idea of the contribution of AGN to the cosmic X-ray

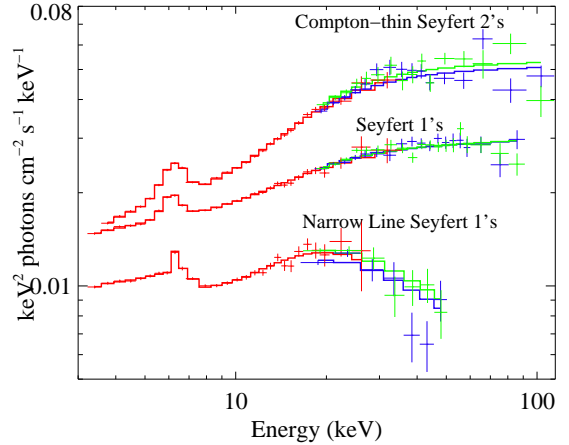


FIG. 7.— Stacked X-ray  $\nu F_\nu$  spectra for Seyfert 1's (excluding NLSy1's), Compton thin Seyfert 2's (excluding Cen A), and Narrow Line Seyfert 1's. Red, blue and green data points and model lines denote PCA, HEXTE-A, and HEXTE-B. We found best fit photon index values of  $1.85 \pm 0.02$ ,  $1.77 \pm 0.03$  and  $2.18 \pm 0.08$  for Seyfert 1's, 2's and NLSy1's respectively. Values of  $R$  from the stacked spectra were found to be  $0.5 \pm 0.1$ ,  $1.1 \pm 0.1$ , and  $1.5 \pm 0.7$ . For the NLSy1's, the peak around 20 keV is the CRH which shows up clearly above the downward sloping power law.

background (CXB; see, e.g., Gilli et al. 2007). The individual spectra used to create the stacked spectra were not put into local reference frames, however blurring of the Fe line and edge due to our including sources spanning a range of redshifts was less than the energy resolution of the PCA. These stacked spectra are shown in Figure 7 as  $\nu F_\nu$  plots, giving the X-ray portion of the spectral energy distribution (SED) and clearly showing the difference in spectral shape between NLSy1's and other Seyferts.

Results of fitting the base model to these spectra yielded average photon indices of  $1.85 \pm 0.02$ ,  $1.77 \pm 0.03$  and  $2.18 \pm 0.08$  for Seyfert 1's, 2's and NLSy1's respectively. Values of  $R$  from the stacked spectra were found to be  $0.5 \pm 0.1$ ,  $1.1 \pm 0.1$ , and  $1.5 \pm 0.7$ . Absorption in the line of sight was not significant to include in any of the sub-sets. Even though many Seyfert 2's show significant absorption  $> 10^{22}$   $\text{cm}^{-2}$ , the soft end of the Compton-thin Seyfert 2 stacked spectrum seems to be dominated by NGC 5506, which has a relatively high flux, long exposure time, and a very low column density. Note that these fitted parameters are significantly higher than our average unweighted values in Table 7. This demonstrates that weighting is an important factor in CXB synthesis models, even within a given type of object, due to the high variation among these sources. In any given patch of the sky, the portion of the CXB due to unresolved AGN could vary in spectral shape due to individual sources. We will base the remainder of our discussion on our sample averages from Table 7 which give equal weight to all objects and are therefore not dominated by the most-observed/brightest sources.

Figures 8 and 9 show the relationship between luminosity and photon index for our Seyfert sample. We converted the X-ray luminosity to bolometric luminosity ( $L_{\text{Bol}}$ ) using a luminosity-dependent scaling factor from Marconi et al. (2004). Eddington luminosity ( $L_{\text{Edd}}$ ) values were computed from black hole masses for 49 sources, primarily taken from Vestergaard & Peterson (2006), and when not present there, from Winter et al. (2009) and Merloni et al. (2003). We do not find a significant correlation between  $\Gamma$  and  $L_{2-10}$  or  $\Gamma$  and  $L_{\text{Bol}}/L_{\text{Edd}}$ . Sobolewska & Papadakis (2009) analyzed *RXTE* monitoring data of 10 AGN and found that for a given AGN,

TABLE 8  
COMPARISONS TO SELECTED SURVEYS: AVERAGE SPECTRAL PARAMETER VALUES

	This Work	Dadina08	Patrick12	Ricci11	Nandra94	Gondek96	Winter09
All Seyferts ..... $\Gamma$	1.90	1.8			1.95		1.78
..... $R$	0.45	1.0			1.60		
Seyfert 1's ..... $\Gamma$	1.86	1.89*	1.82	1.96		1.90	
..... $R$	0.27	1.23*		0.2		0.76	
Narrow Line Seyfert 1's ..... $\Gamma$	2.24			2.28			
..... $R$	0.89			4.3			
Compton-thin Seyfert 2's ..... $\Gamma$	1.85	1.80*		1.97			
..... $R$	0.27	0.87*		2.0			
Compton-thick Seyfert 2's.... $\Gamma$	1.40			1.9			
..... $R$	0.48			1.4			

NOTE. — Comparing our average spectral parameters to several other surveys of Seyferts in the hard X-ray band. We find that we are consistent in general with other surveys though a number of specific cases of discrepancies highlight that the high variance among Seyferts means that the makeup of any given sample is important. In particular Dadina (2008) did not separate out NLSy1's or Compton-thick versus Compton-thin Seyfert 2's. The energy band and analysis methods can also have a strong influence on measured values of  $R$  as demonstrated by our fitted values to stacked spectra versus equally weighted averages (see Section 4.1). The "\*" symbol indicates averages that may not separate NLSy1's from the typical Seyfert 1's or Compton-thick Seyfert 2's from the Compton-thin Seyfert 2's. The other surveys are Dadina (2008), Patrick et al. (2012), Ricci et al. (2011), Nandra & Pounds (1994), Gondek et al. (1996), and Winter et al. (2009).

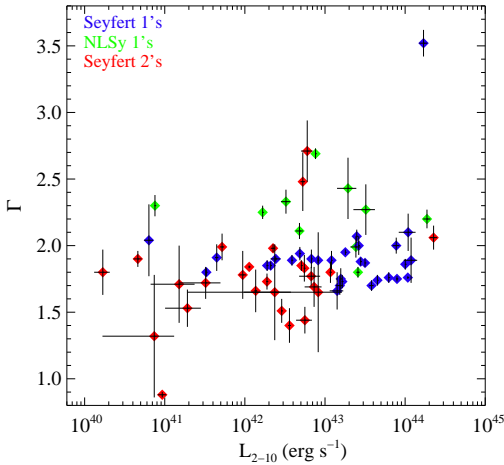


FIG. 8.— The photon index showed no significant correlation with the 2–10 keV unabsorbed X-ray luminosity.

$\Gamma$  is correlated with both  $F_{2-10}$  and the mass accretion rate,  $\dot{m}_{X,E}$  ( $L_{2-10}/L_{\text{Edd}}$ ), and that across their sample there was a positive correlation between  $\Gamma$  and  $\dot{m}_{X,E}$ . We do not see this trend across our entire sample of AGN. This could be due to a number of factors, for instance their objects were all quite bright and one of them, Ark 564, lies at one extreme corner of the  $\Gamma$  versus Eddington ratio plot in Figure 9. We do not find a correlation between  $\Gamma$  and  $L_{\text{Bol}}/L_{\text{Edd}}$  for the other nine objects in their sample (note that our black hole masses were not identical to theirs and this happens to lessen the correlation considerably as well).

#### 4.2. Comparisons to Previous Surveys

A large number of X-ray spectral surveys of AGN have been performed in the past, with anywhere from a small handful to over one hundred objects, and with a variety of energy ranges. Average values of  $\Gamma$  and  $R$  for several surveys which included data above 10 keV are given in Table 8.

Dadina (2008) performed a survey on 105 Seyferts with

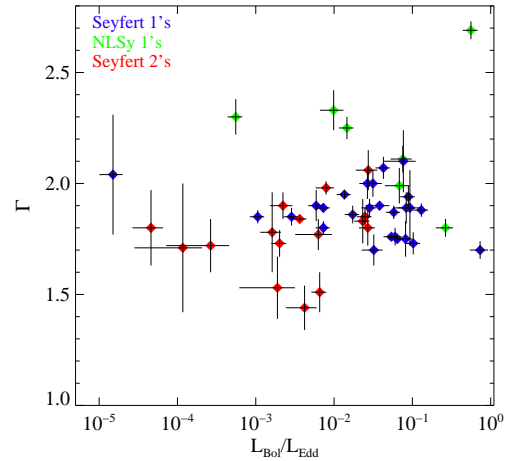


FIG. 9.— Photon index versus Eddington ratio showed no significant correlation. Black hole masses were obtained for 49 sources primarily from Vestergaard & Peterson (2006), and when not present there, from Winter et al. (2009) and Merloni et al. (2003). Converting our X-ray luminosity to bolometric luminosity we used a luminosity-dependent scaling factor from Marconi et al. (2004).

*BeppoSAX* data in the 2–100 keV range, finding average values of  $\Gamma \sim 1.8$ ,  $R \sim 1.0$ , and  $E_{\text{roll}} \sim 290$  keV. Their average photon index is lower than ours, likely due to their inclusion of high energy rollovers which would tend to cause slightly their slightly flatter values of  $\Gamma$ . We did not do an extensive search for high energy rollovers in this sample since previous work has already been done with the highest quality HEXTE data (RMR2011) which ruled out the presence of a rollover below 200 keV in most cases. Their exceptionally high average  $R$  value for Seyfert 1's of 1.23 is less easy to explain. Additionally, Dadina (2008) found correlations between  $\Gamma$  and  $R$ , and between  $L_{2-10}$  and the  $EW$  of the neutral Fe  $K\alpha$  line, the ‘‘X-ray Baldwin Effect,’’ neither of which could be confirmed in our data. Again, the inclusion of several Compton-thick sources could have an effect given the degeneracy in measuring  $\Gamma$  and  $R$  in these sources.

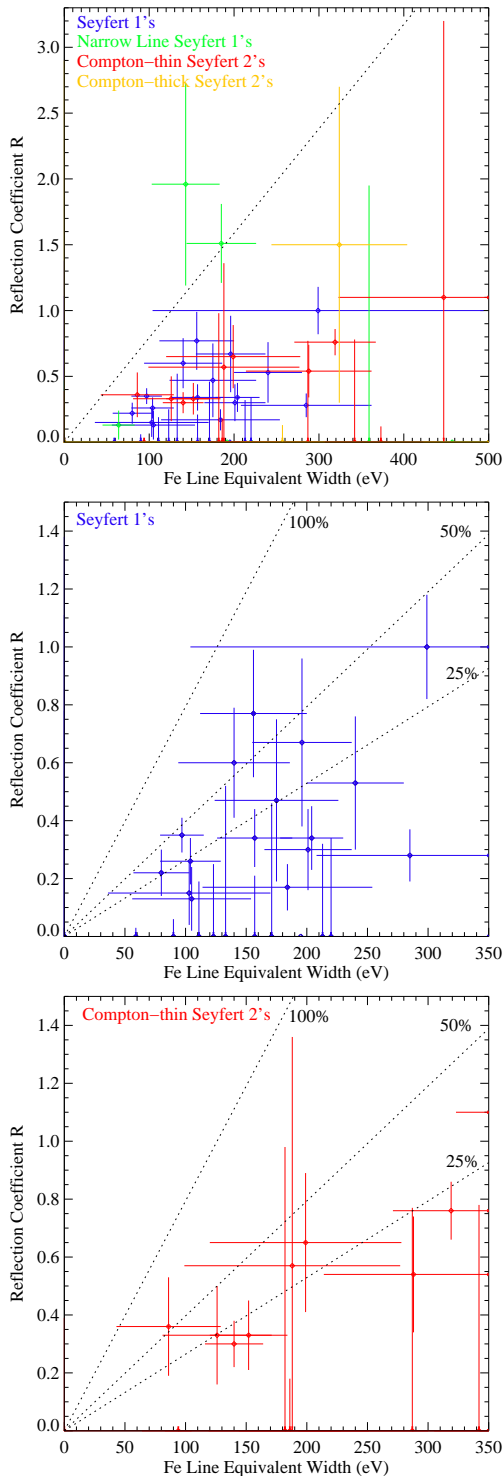


FIG. 10.— Comparing the amount of reflection,  $R$ , to the EW of the Fe  $K\alpha$  line for Seyfersts. The left-most dashed line is the predicted amount of Fe emission associated with reflection off Compton-thick material in a disk. Points falling the right of this line must have additional contribution from Compton thin material. The dashed lines indicate the relative amount of Fe line flux contributed by Compton-thick material. Seyfert 1's and Compton-thin Seyfert 2's have been isolated in the bottom panels for clarity. Note the different axis ranges for these panels and that no sources with  $EW > 500$  eV are included here.

Patrick et al. (2012) analyzed a sample of 46 Seyfert 1's observed with *Suzaku* and *Swift*-BAT and found that 39 out of their 46 Seyfert 1's showed a significant CRH, exactly in line with our 85% of sources. However since they used a different Compton reflection model we cannot directly compare our  $R$  values with their results, necessitating an alternative measurement of the strength of the CRH, as detailed in the following section. They found an average  $\Gamma$  for their sample of  $1.82 \pm 0.03$ , in agreement with our value for Seyfert 1's of  $1.86 \pm 0.27$ . Their inclusion of Seyfert 1.8–1.9 in their sample should not have an effect on this value since we find that there is no difference in the average value of  $\Gamma$  between Seyfert 1–1.5's and Compton thin Seyfert 1.8–2's.

Other surveys have been performed with more limited energy ranges and/or fewer objects. A survey of Seyfersts at high X-ray energies was done by Ricci et al. (2011) using stacked *INTEGRAL*-ISGRI data in the 17–250 keV range for different classes of Seyfersts to obtain bulk spectral properties. Discrepancies between their results and ours may be due to their lack of coverage below 17 keV, making it difficult to quantify the underlying power law in sources with strong Compton reflection, modeling of the CRH (assumptions about inclination angle can change measured  $R$  values), and stacking itself, which as we have discussed above can lead to domination by just a few sources. They also fitted their spectra with models that included high energy rollovers in the 100–300 keV range. When they modeled high energy rollovers their average  $\Gamma$  and  $R$  values for Seyfersts 1's were 1.8 and 0.1, for Compton-thin Seyfert 2's 1.6 and 0.4, for Compton-thick Seyfert 2's 1.9 and 1.4, and for NLSy1's 2.3 and 4.2, demonstrating the degeneracy between  $\Gamma$ ,  $R$  and  $E_{\text{roll}}$ .

Nandra & Pounds (1994) analyzed *Ginga* data of 27 Seyfersts in the 1.5–37 keV range and found average  $\Gamma$  and  $R$  values of 1.95 and 1.60. Gondek et al. (1996) produced stacked Seyfert 1 spectra using combined *CGRO*-OSSE, *Ginga* and *EXOSAT* data (taken at different times) with average values for  $\Gamma$  and  $R$  of  $1.90 \pm 0.05$  and  $0.76 \pm 0.15$ . Both these samples are consistent with our average values for the entire sample of 1.9 and 0.54 respectively. Winter et al. (2009) found an average  $\Gamma$  of 1.78 with a standard deviation of 0.24 for a sample of 102 *Swift*-BAT selected AGN, however they did not model any Compton reflection.

Our *RXTE* results are consistent with previous analyses and our sample has a number of advantages over previous surveys in the medium–hard X-ray bandpass. Since the PCA and HEXTE have always operated simultaneously, we do not have the ambiguity from source variability that comes from combining non-simultaneous soft and hard X-ray data sets from different missions as is commonly necessary to obtain broad-band coverage. The broad bandpass is necessary to accurately constrain Compton reflection and gain insight into the geometry and characteristics of the circumnuclear material. Additionally, many of these sources were monitored over long periods of time and for these sources the spectral parameters can be taken as good longterm average baselines for time-resolved spectral analysis.

#### 4.3. The Circumnuclear Material

There are a number of factors that affect the shape and relative strength of the CRH: the photon index of the incident power law, the inclination angle, the covering fraction of the material relative to the illuminating source, elemental abundances, and the geometry of the reflecting material. Unfortunately, the changes in shape are very subtle and high en-

ergy spectrometers are not sensitive enough to these subtle differences to deconvolve all of these effects through spectral modeling. This has led to simplifications in the models and assumptions about the geometry of the reflecting material. Common CRH models in use typically assume either a flat disk or a uniform torus, but since both produce such similar spectral signatures, we must use other techniques to discern the geometry of the Compton thick material.

The PEXRAV model has been widely used to model reflection off a disk of Compton thick material such as the accretion disk. It assumes a plane of Compton-thick material covering between 0 and  $\sim 2\pi$  steradians of the sky from the point of view of the illuminating source corresponding to  $R$  between 0 and  $\sim 1$ . However, a number of objects in our sample have reflection fractions greater than 1, which is unphysical in this model, as is freezing the inclination angle to  $30^\circ$  for all objects. It may seem tempting at this point to choose more accurate inclination angles on an object by object basis, however accurate estimates are very difficult to come by. It is sometimes assumed, based on Seyfert 1/2 unification schemes, that Seyfert 1's will have smaller inclination angles (i.e. "face on" to the observer) while Seyfert 2's will have larger angles (i.e. "edge on" to the observer), but this poses a number of problems. The first is that if we assume these objects have inherent differences we will inevitably find that we are correct. For example assuming Seyfert 2's are on average at an angle of  $60^\circ$  will inflate the value of  $R$  by a factor of 1.2–1.5, leading to the possibly erroneous conclusion that there is more Compton thick material surrounding Seyfert 2's.

Additionally, this does not take into account what effect a torus may have if present. We attempted to apply the torus model MYTORUS (Murphy & Yaqoob 2009) to our data. This model is a simple donut shape of uniform density with an opening angle of  $60^\circ$ . Unfortunately, the model's assumption that the torus has a uniform density leads to a steep change in the line-of-sight absorption at the edge of the donut-shaped torus, causing all Compton-thin sources to have fitted inclination angles close to  $60^\circ$ . Most sources also required additional Fe line emission from Compton-thin material, which meant that the Fe line could not be used to constrain the amount of Compton-thick material in these sources. For the majority of our sources this led to two parameters, angle and torus density, to characterize only one measurable quantity: the flux of the CRH.

We concluded that the best way to proceed was with the results of the PEXRAV model, but to utilize it in a predominantly phenomenological way. Since PEXRAV is not the only CRH model available, we also report the flux ratios in Tables 2–4, the relative flux of the CRH to the underlying power law near the peak of the CRH between 15 and 50 keV, which we can use to compare to results using other models, including ionized reflectors, such as REFLIONX, or torus models such as MYTORUS. We calculated this flux ratio ( $FR$ ) by finding the 15–50 keV flux for the power law continuum and for the CRH, then defining  $FR = F_{\text{CRH}}/F_{\text{cont}}$ . There is a linear proportionality between  $FR$  and  $R$  for fixed values of  $\cos i$  and  $\Gamma$ . At  $30^\circ$  with  $\Gamma = 1.9$ , we find that  $FR = 0.8R$ . Patrick et al. (2012) reported  $FR$  values for their 46 Seyfert 1's modeled with REFLIONX. Comparing their distribution of reflection fractions (their Figure 12) with ours, shown in Figure 5, we see a very similar smooth distribution with the majority of objects falling below  $R=1$  ( $FR=0.8$ ) but with a long tail towards higher values.

Using the Kolmogorov-Smirnov Test to compare our dis-

tributions of  $R$  for Seyfert 1's versus Seyfert 2's we find a  $P$  value of 0.999 ( $P=0.982$  comparing distributions of  $FR$ ), where we have ignored the outliers NGC 6240, Circinus and NGC 4945, and included only well-determined  $R$  values (i.e., with  $\sigma_R/R > 1$  and upper limits  $< 0.5$ ). Here,  $P$  denotes the likelihood that the two distributions of values of  $R$  (or  $FR$ ) can arise from the same parent population and thus confirms that the distributions are statistically similar between both classes of objects. These distributions are likely not consistent with the simple disk geometry and the standard Seyfert 1/2 unification since we would expect to see more Compton reflection in face-on Seyfert 1's than in side-view Seyfert 2's, which we do not observe. The similarity in reflection fractions in our Seyfert 1's and 2's is consistent with reflection off the inner wall of a torus, where viewing angle does not change the amount of observed reflection significantly. We tested this empirically using the MYTORUS and PEXRAV models and found a factor of  $\lesssim 10\%$  difference in  $FR$  going from  $0^\circ$  viewing angle to  $60^\circ$  for the torus, in contrast to a factor of  $\sim 40\%$  difference over the same angle change for a disk. At viewing angles greater than  $\sim 60^\circ$  obscuration from the torus becomes a factor.

Another way to probe the circumnuclear material is to compare the strength of the Fe line with the strength of the Compton hump. George & Fabian (1991) calculated the expected flux of the Fe line produced by reflection off a Compton-thick disk with respect to the flux of the Compton hump; it's expected that the Fe line EW will be  $\sim 150$  eV for  $R \sim 1$  at an angle of  $30^\circ$ . In Figure 10 we show the strength of the CRH plotted versus the EW of the Fe line for all Seyferts. From our analysis, Compton-thick reflection accounts for  $\sim 40\%$  of the Fe line flux on average, however the variation is quite large. The remainder of the Fe line flux may arise in Compton-thin neutral gas in the NLR or in the BLR clouds (although there is a limit to how much Fe line flux Compton-thin gas can produce; see De Rosa et al. 2012) and/or be from ionized Compton-thin gas in the vicinity of the nucleus. With the limited resolution of the PCA around 6–7 keV we cannot disentangle these possible origins. Approximately three quarters of Seyfert 1's and Compton-thin 2's show more Fe line flux from sources other than from Compton reflection, assuming a disk geometry. Note that Compton-reflection from a torus may have a slightly different expected ratio of the Fe line to the CRH flux, depending on the particular geometry assumed.

#### 4.4. Results for the Blazar Sample

Most of the blazars in our sample were well fit by a simple power law. Four BL Lac type objects were fit better by a broken power law with break energies below  $\sim 10$  keV and steepening by  $\sim 0.2$  (note that this small a change in  $\Gamma$  is due to a very gradual rollover of the spectrum which we are only sensitive to in our brightest sources). The average  $\Gamma$  for our sample was 2.1 with a variance of 0.15. The average  $\Gamma$  for flat spectrum radio quasars (FSRQ's) was 1.8 while the average for BL Lac objects was 2.3 with variances of 0.2 and 0.1 respectively. The distribution of  $\Gamma$  for the blazar sub-types is shown in Figure 11.

In addition to the lower photon index, the FSRQ's also tend to be much more luminous than the BL Lac's. Figure 12 shows the X-ray 2–10 keV luminosity versus the photon index for our sample of blazars. We found a weak anti-correlation between these quantities with a Pearson correlation coefficient of  $-0.40$ , significant at the 99% level. This is consistent with the "Fossati sequence" (Fossati et al. 1998) which predicts



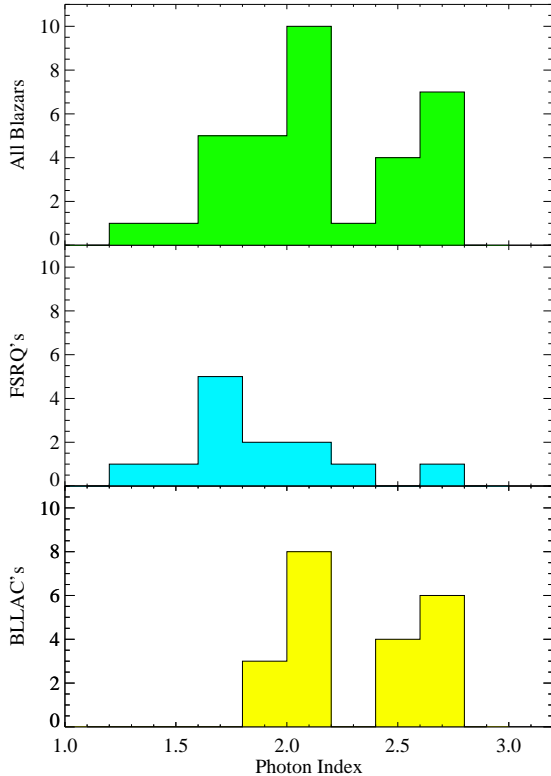


FIG. 11.—  $\Gamma$  distribution by blazar type. BL Lac objects tend to have higher photon indices than FSRQ's.

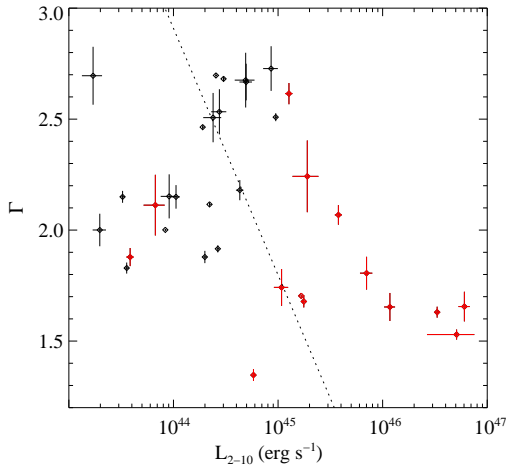


FIG. 12.— Photon index versus 2–10 keV luminosity for the blazars in our sample. Red data points are FSRQ's; black data points are BL Lac objects. We find significant negative correlation which is consistent with the Fossati sequence.

that for higher luminosities the peak of the broadband emission humps would shift to lower energies. At lower luminosities the upper end of the synchrotron hump dominates the X-ray band while at higher luminosities the lower end of the inverse Compton hump dominates. This means a softening of the X-ray portion of the SED and an increase in the photon index as luminosity decreases. Donato et al. (2001) published a large X-ray sample of blazars observed by *BeppoSAX* which also confirmed this trend.

Dai & Zhang (2003) analyzed *EXOSAT*, *ASCA* and *BeppoSAX* data to obtain hard X-ray photon indices for 20

sources. They reported average  $\Gamma$  of  $2.78 \pm 0.25$  for high-frequency-peaked BL Lac objects (HBLs),  $1.85 \pm 0.35$  for low-frequency-peaked BL Lac objects (LBLs), and  $1.64 \pm 0.28$  for FSRQs. Fan et al. 2012 focused on Fermi-selected blazars, finding average values of  $\Gamma$  in the X-ray band of  $2.39 \pm 0.35$  for HBLs,  $1.97 \pm 0.38$  for LBLs, and  $1.89 \pm 0.37$  for FSRQs. Noting that the majority of our BL Lac objects are high-frequency or intermediate-frequency peaked, these measurements are all in good agreement with ours.

#### 4.5. Conclusion

We have analyzed data for 100 AGN in the *RXTE* archive in order to explore the geometry of circumnuclear material around SMBH's and characterize their X-ray spectra. We present a large sample of X-ray bright AGN which has a number of advantages over previous surveys in the medium-hard X-ray bandpass: the simultaneity of the  $<10$  keV and  $>10$  keV X-ray data eliminates ambiguity, the relatively broad bandpass is necessary to accurately measure the continuum power law and the CRH in order to gain insight into the geometry and characteristics of the circumnuclear material, and the long monitoring campaigns make this sample ideal for using as a baseline average for future time-resolved spectral analysis. To that end, we have presented the spectral parameters of our sample including absorption, Fe line equivalent widths, Compton reflection strengths, photon indices, and 2–10 keV fluxes in Tables 2–6 along with average values by type in Table 7.

The similar distributions of  $\Gamma$  for type 1 and 2 Seyferts supports the idea that they share a common central engine. The distribution of  $R$  showed no difference in the reflection from Compton-thick material in Seyfert 1's and 2's. This is counter to what we would expect from reflection off a disk under classical unification schemes where face-on Seyfert 1's would be expected to show significantly more reflection than edge-on Seyfert 2's. The similar distributions are more consistent with reflection off a torus. We did not find a significant correlation between  $\Gamma$  and  $L_{2-10}$  for the Seyferts in our sample, however NLSy1's showed significantly higher photon indices. This is consistent with a common central engine for all Seyferts with the primary differences between types being dependent on accretion rate and the geometry of the circumnuclear material. Additionally, a few of the Seyfert 2's in our sample had very soft X-ray spectra, similar to NLSy1's, and could be type 2 analogs of NLSy1's, as expected under unification.

We found that roughly 85% of Seyferts showed significant contribution from the CRH. Comparing the strength of the CRH with the amount of the Fe emission seen allowed us to estimate the ratio of Compton-thick to Compton-thin material in AGN with the average being around 40%, however with large object to object variation.

We found a negative correlation between  $\Gamma$  and  $L_{2-10}$  for blazars in agreement with the Fossati sequence and the luminosity dependence of the broad band SED hump peak energies.

We confirm that it is likely AGN do share a common engine across the various types, concluding that the differences in their observed properties are likely based on mass, accretion rate, and geometry of the circumnuclear material. The ratio of Compton-thick to Compton-thin material was not consistent from object to object and did not seem to be dependent on optical classification. While Seyfert 2's were more likely to have high absorption columns, they were as likely to show

strong Compton reflection humps as Seyfert 1's, inconsistent with reflection off a disk, assuming type depends on inclination angle. A more complex reflecting geometry such as a torus, combined disk and torus, or clumpy torus is likely a more accurate picture of the Compton-thick material.

As a resource for future analyses of AGN, we plan to make spectra and light curves available online. These spectra may serve as baselines for future missions such as *NuSTAR*, which will look at a large number of AGN in the 6–80 keV band with excellent sensitivity and spectral resolution. They could potentially be combined with multi-wavelength data to create SED's for future analysis or with information about abundances of the different types to create the AGN contri-

bution to the CXB.

The authors would like to thank Joern Wilms and Craig Markwardt for valuable advice, as well as the anonymous referee for their diligence and patience. This research has made use of data obtained from the *RXTE* satellite, a NASA space mission. This work has made use of HEASARC online services, supported by NASA/GSFC, and the NASA/IPAC Extragalactic Database, operated by JPL/California Institute of Technology under contract with NASA. The research was supported by NASA Contract NAS 5-30720 and Grants NNX09AG79G and NNX11AD07G.

## REFERENCES

- Antonucci R., 1993, *ARA&A*, 31, 473  
 Awaki, H., Murakami, H., Leighly, K.M., Matsumoto, C., Hayashida, K. & Grupe, D. 2005, *ApJ*, 632, 793  
 Bianchi, S., Chiaberge, M., Piconcelli, E., Guainazzi, M. 2007, *MNRAS*, 374, 697  
 Bianchi, S., Miniutti, G., Fabian, A.C., Iwasawa, K., 2005, *MNRAS*, 360, 380  
 Bianchi, S., Piconcelli, E., Chiaberge, M., Jiménez Bailón, Matt., G. & Fiore, F. 2009, *ApJ*, 695, 781  
 Blustin, A. J., Page, M. J., Fuerst, S. V., Branduardi-Raymont, G., Ashton, C. E. 2005, *A&A*, 431, 111  
 Colbert, E.J. M., Weaver, K.A., Krolik, J.H., Mulchaey, J.S., Mushotzky, R.F. 2002, *ApJ*, 581, 182  
 Dadina, M. 2007, *A&A*, 461, 1209  
 Dadina, M. 2008, *A&A*, 485, 417  
 Dai, B.Z. & Zhang, L. 2003, *PASJ*, 55, 939  
 de Rosa, A. et al. 2012, *MNRAS*, 420, 2087  
 Donato, D., Ghisellini, G., Tagliaferri, G., & Fossati, G. 2001, *A&A*, 375, 739  
 Elvis, M., Maccacaro, T., Wilson, A.S., Ward, M.J., Penston, M.V., Fosbury, R.A.E., & Perola, G.C. 1978, *MNRAS*, 183, 129  
 Fabian, A.C., Sanders, J.S., Taylor, G.B., Allen, S.W., Crawford, C.S., Johnstone, R.M., & Iwasawa, K., 2006, *MNRAS*, 366, 417  
 Fan, J. H., Yang, J. H., Yuan, Y. H., Wang, J., Gao, Y. 2012, *ApJ*, 761, 125  
 Fossati, G., Maraschi, L., Celotti, A., Comastri, A., & Ghisellini, G. 1998, *MNRAS*, 299, 433  
 George, I.M., & Fabian, A.C. 1991, *MNRAS*, 249, 352  
 Gilli, R., Comastri, A. & Hasinger, G. 2007, *A&A*, 463, 79  
 Gondek, D., Zdziarski, A.A., Johnson, W.N., et al. 1996, *MNRAS*, 282, 646  
 Grandi, P., Guainazzi, M., Mineo, T., et al., 1997, *A&A*, 325, L17  
 Grupe, D., Beuermann, K., Mannheim, K., & Thomas, H.-C. 1999, *A&A*, 350, 805  
 Guainazzi, M. 2002, *MNRAS*, 329L, 13  
 Jahoda, K., Markwardt, C.B., Radeva, Y., Rots, A.H., Stark, M.J., Swank, J.H., Strohmayer, T.E., Zhang, W., 2006, *ApJS*, 163, 401  
 Kalberla, P.M.W., Burton, W.B., Hartmann, Dap, Arnal, E.M., Bajaja, E., Morras, R., & Pöppel, W.G.L., 2005, *A&A*, 440, 775  
 Kataoka, J., Tanihata, C., Kawai, N., Takahara, F., Takahashi, T., Edwards, P.G. & Makino, F. 2002, *MNRAS*, 336, 932  
 Komossa, S., Burwitz, V., Hasinger, G., Predehl, P., Kaastra, J. S., Ikebe, Y. 2003, *ApJ*, 582L, 15  
 Leighly, Karen M., Halpern, Jules P., Awaki, Hisamitsu, Cappi, Massimo, Ueno, Shiro, Siebert, Joachim 1999*ApJ*, 522, 209  
 Lira P., Ward M.J., Zezas, A., & Murray, S.S. 2002, *MNRAS*, 333, 709  
 Magdziarz, P. & Zdziarski, A.A. 1995, *MNRAS*, 273, 837  
 Matt, G., Bianchi, S., Guainazzi, M., Molendi, S. 2004, *A&A*, 414, 155  
 Matt, G. et al. 1999 *A&A*, 341, L39  
 Matt, G. et al. 1997, *A&A*, 325, 13  
 Markowitz, A., Reeves, J. N., George, I. M., Braito, V., Smith, R., Vaughan, S., Arévalo, P., Tombesi, F. 2009, *ApJ*, 691, 922  
 McKernan, B., Yaqoob, T. & Reynolds, C.S. 2007, *MNRAS*, 379, 1359  
 Merloni, A., Heinz, S., & di Matteo, T. 2003, *MNRAS*, 345, 1057  
 Marconi, A., Risaliti, G., Gilli, R., Hunt, L. K., Maiolino, R., & Salvati, M. 2004, *MNRAS*, 351, 169  
 Mukai, K., Hellier, C., Madejski, G., Patterson, J., & Skillman, D.R. 2003, *ApJ*, 597, 479  
 Murphy, K. D. & Yaqoob, T., 2009, *MNRAS*, 397, 1549  
 Nagar, N.M., Oliva E., Marconi A., Maiolino R., 2002, *A&A*, 391, L21  
 Nandra, K. & Pounds, K. A., 1994, *MNRAS*, 268, 405  
 Nandra, K., Le, T., George, I.M., Edelson, R.A., Mushotzky, R.F., Peterson, B.M., & Turner, T.J. 2000, *ApJ*, 544, 734  
 Netzer, H. et al. 2003, *ApJ*, 599, 933  
 Patrick, A.R., Reeves, J.N., Porquet, D., Markowitz, A.G., Braito, V. & Lobban, A.P. *MNRAS*, 426, 2522  
 Pounds, K., Done, C., & Osborne, J.P. 1995, *MNRAS*, 277, 5  
 Pounds, K. A., King, A. R., Page, K. L., O'Brien, P. T. 2003, *MNRAS*, 346, 1025  
 Ramos Almeida, C., et al. 2011, *ApJ*, 731, 92  
 Ricci, C., Walter, R., Courvoisier, T.J.-L. & Paltani, S. 2011, *A&A*, 532, 102  
 Rivers, E., Markowitz, A., & Rothschild, R.E. 2011, *ApJS*, 193, 3  
 Rothschild R.E., et al. 1998, *ApJ*, 496, 538  
 Sako, M., Kahn, S.M., Paerels, F., & Liedahl, D.A. 2000, *ApJ*, 543, 115  
 Sambruna, R.M. et al., 2001, *ApJ*, 546, L13  
 Schurch, N.J., Roberts, T. P., & Warwick, R.S., 2002, *MNRAS*, 335, 241  
 Sobolewska, M.A., & Papadakis, I.E., 2009, *MNRAS*, 339, 1597  
 Steenbrugge, K. et al. 2003, *A&A*, 408, 921  
 Steenbrugge, K. et al. 2005, *A&A*, 434, 569  
 Tueller, J. 2010, *ApJS*, 186, 378  
 Turner, T.J., Reeves, J.N., Kraemer, S.B., & Miller, L. 2008, *A&A*, 483, 161  
 Turner, T. J., Perola, G. C., Fiore, F., Matt, G., George, I. M., Piro, L., Bassani, L. 2000*ApJ*, 531, 245  
 Verner, D. A., Ferland, G. J., Korista, K. T., & Yakovlev, D.G. 1996, *ApJS*, 465, 487  
 Vestergaard, M. & Peterson, B. 2006, *ApJ*, 641, 689  
 Walton, D. J., Nardini, E., Fabian, A. C., Gallo, L. C., Reis, R. C. 2013, *MNRAS*, 428, 2901  
 Wilms, J., Allen, A., & McCray, M. 2000, *ApJ* 542, 914  
 Winter, L.M., Mushotzky, R.F., Reynolds, C.S., & Tueller, J. 2009, *ApJ*, 690, 1322  
 Yang, Y., Wilson, A. S., Matt, G., Terashima, Y., Greenhill, L. J., 2009, *ApJ*, 691, 131  
 Zdziarski, A.A., Poutanen, J. & Johnson, W.N. 2000, *ApJ*, 542, 703

## APPENDIX

### A. REJECTED SOURCES

Approximately 60 AGN were observed in the lifetime of *RXTE* which are not included in our sample. Most of them were very faint and/or were not observed for very long. A few objects were contaminated by other X-ray bright sources in the field of view. For example, 3C 84 is known to be embedded in an X-ray bright galaxy cluster (e.g., Fabian et al. 2006) whose emission dominated the PCA spectrum. Observations of NGC 6814 have the cataclysmic variable V1432 Aql in the field of view (Mukai et al. 2003). Observations of the blazar RGB J1217+301 were consistent with detecting only contaminating flux from the NLSy1 Mkn 766 and the blazar 1ES 1218+304, located approximately 0.33 and 0.76 degrees away, respectively. The remaining AGN are listed in Table 9 including their type as determined by NED, PCA exposure time,  $F_{2-10}$ , and  $\Gamma$  where it was possible to constrain.



TABLE 9  
OTHER AGN IN THE *RXTE* ARCHIVE

Source Name	Type	PCA Exposure (ks)	Flux <sub>2-10</sub> ( $10^{-12}$ erg cm <sup>-2</sup> s <sup>-1</sup> )	$\Gamma$
Seyfert 1's				
H0147-537	QSO	83.3	$2.7 \pm 0.1$	$1.9 \pm 0.2$
1H 0707-495	NLSy1	7.8	$4.3 \pm 1.7$	$3.5 \pm 0.5$
LBQS 2212-1759	BALQSO	18.3	$1.4^{+0.1}_{-0.4}$	$2.3 \pm 0.5$
PG 1116+215	Sy1	51.1	$3.5 \pm 0.1$	$1.83 \pm 0.11$
PG 1416-129	Sy1	22.4	$3.7 \pm 2.4$	$1.5 \pm 0.3$
PG 1440+356 (Mkn 478)	NLSy1	27.9	$3.2^{+0.1}_{-0.3}$	$2.8 \pm 0.3$
PG 1700+518	Sy1/BALQSO	27.4	$< 0.2$	-
RHS 03	Sy1	7.0	$8.2 \pm 6.3$	$1.9 \pm 0.2$
RHS 15	Sy1	9.8	$2.6 \pm 0.2$	$1.0 \pm 0.2$
RHS 17	Sy1	9.9	$7.5 \pm 1.6$	$1.6 \pm 0.2$
RHS 54	Sy1	7.4	$1.8^{+0.2}_{-0.6}$	$1.2 \pm 0.5$
RHS 56	NLSy1	10.2	$5.8 \pm 0.8$	$2.2 \pm 0.2$
RHS 61	Sy1	8.9	$4.8 \pm 1.7$	$1.9 \pm 0.3$
TON1542 (Mkn 771)	Sy1	90.9	$3.8 \pm 0.1$	$2.0 \pm 0.1$
Seyfert 2's				
Arp 220	Sy2/ULIRG	0.9	$< 1.5$	-
E 253-G3	Sy2	1.7	$3.7 \pm 3.7$	$0.9 \pm 0.6$
IRAS F00521-7054	Sy2	1.5	$4.2^{+0.4}_{-2.1}$	$1.6 \pm 0.5$
IRAS F01475-0740	Sy2/ULIRG	3.0	$< 1.3$	-
IRAS F03362-1642	Sy2	1.8	$< 1.3$	-
IRAS F04385-0828	Sy2	1.9	$4.7^{+0.5}_{-2.8}$	$1.6 \pm 0.4$
IRAS F05189-2524	Sy2/ULIRG	1.4	$< 3.3$	$1.9^{+0.9}_{-0.8}$
IRAS F08572+3915	Sy2/ULIRG	3.4	$< 2.7$	$1.9 \pm 0.7$
IRAS F19254-7245 (AM 1925-724)	Sy2	1.8	$< 1.5$	-
MCG-3-34-63	Sy2	1.8	$1.8 \pm 1.8$	-
NGC 1320	Sy2	3.4	$< 0.9$	-
NGC 1386	Sy2	2.5	$5.8 \pm 2.3$	$2.7 \pm 1.0$
NGC 3281	Sy2/C-thick	11.4	$8.0 \pm 2.4$	$2.6 \pm 1.5$
NGC 3660	Sy2	3.2	$< 2.0$	$1.8^{+0.9}_{-0.8}$
NGC 5347	Sy2	3.2	$< 1.8$	$1.7^{+1.0}_{-0.9}$
NGC 6251	Sy2	148	$3.2^{+0.1}_{-0.4}$	$2.38 \pm 0.23$
NGC 6394	Sy2	23.8	$< 1.9$	-
NGC 6890	Sy2	2.5	$1.1 \pm 0.3$	$0.9 \pm 1.3$
TOL 1238-364 (IC 3639)	Sy2	1.7	$< 1.4$	$2.9^{+3.1}_{-1.7}$
Blazars				
0420-014	BLLAC	1.0	$< 2.8$	-
1ES 0806+524	BLLAC	39.4	$5.6^{+0.3}_{-0.8}$	$2.8 \pm 0.2$
3C 446	BLLAC	40.5	$< 1.5$	$2.0 \pm 0.6$
4C 38.41	FSRQ	65.5	$1.7^{+0.2}_{-0.5}$	$1.45 \pm 0.30$
H 2356-309	BLLAC	2.2	$8^{+2}_{-7}$	$2.4 \pm 0.5$
O J287	BLLAC	116.8	$< 0.2$	-
PG 1424+240	BLLAC	32.0	$2.6^{+0.1}_{-0.4}$	$3.6 \pm 0.5$
PKS 0235+164	BLLAC	247.5	$1.6^{+0.3}_{-0.8}$	$2.5 \pm 0.3$
PKS 0332-403	FSRQ	18.8	$3.6^{+0.3}_{-0.6}$	$2.5 \pm 0.4$
PKS 0348-120	FSRQ	93.6	$< 0.1$	-
PKS 0405-385	FSRQ	1.9	$< 0.2$	-
PKS 0537-286	QSO	23.7	$4.1^{+0.1}_{-1.3}$	$1.3 \pm 0.2$
PKS 0537-441	BLLAC	19.3	$3.6^{+0.4}_{-1.5}$	$2.8 \pm 0.5$
PKS 2255-282	FSRQ	5.4	$8.0^{+0.3}_{-0.7}$	$1.67 \pm 0.14$
RGB J0152+017	BLLAC	31.1	$6.4 \pm 0.4$	$2.47^{+0.19}_{-0.18}$
RHS 53	BLLAC	9.2	$3.7^{+0.3}_{-0.3}$	$1.74 \pm 0.23$
W Com (RGB J1221+282)	BLLAC	23.7	$< 1.8$	$1.7 \pm 0.7$

NOTE. — *RXTE* archival AGN which were not included in our main sample with object NED type, PCA exposure time, 2–10 keV flux and  $\Gamma$  where it could be constrained. Where  $\Gamma$  could not be constrained a photon index of 2.0 was assumed to find the upper limit to the flux. Note that the errors given are purely statistical and do not reflect systematic uncertainties in the background. Thus some of these sources may seem to have  $\Gamma$  constrained to within 10% such that they could be included in the sample, however due to low flux or very short exposure the background systematics are large enough that they were not included. “-” indicates an unconstrained parameter. ULIRG is an ultra luminous infrared galaxy and BALQSO is a broad absorption line quasar.

## B. NOTES ON INDIVIDUAL SOURCES

Several sources in our sample required complex modeling or extra analysis. Many Compton-thick sources showed evidence for a soft power law component lacking intrinsic absorption. We have searched through the literature to find explanations for the spectral characteristics of each of these sources.

Circinus is a bright, well-studied, reflection-dominated source with a very strong CRH, a Compton-thick absorber, and a soft power law component, the origin of which is a combination of ionized plasma commensurate with the NLR and contamination from nearby point sources (Matt et al. 1999; Sambruna et al. 2001). We have measured a high energy rollover in this source around  $\sim 40$  keV, consistent with that of  $\sim 50$  keV found by Yang et al. (2009) using *Suzaku*.

The soft power law in Mkn 3 has been identified by Chandra (Sako et al. 2000) and confirmed with *XMM-Newton* (Bianchi et al. 2005) as originating in photoionized plasma in the NLR.

NGC 1068 is a very weak, reflection dominated source and was not observed for only 54 ks by *RXTE*, making it difficult to properly constrain the complex scenarios that have been modeled previously in this source. It was possible to fit this source with with a power law continuum plus a CRH (Table 3) or with a Compton-thick absorber with leaked emission and a CRH (Table 4). Matt et al. (1997) and Colbert et al. (2002) modeled the spectrum below 10 keV with an ionized reflector plus a neutral reflector, however because the source is so faint we cannot distinguish between this and a power law. Since we are unable to place constraints on the Compton-thick absorber in this source due to the extremely high column density and lack of good data above  $\sim 30$  keV, we adopt the parameters from the base model given in Table 3 for this source.

NGC 4945 was best fit by a hard X-ray power law with a Compton-thick absorber and an additional power law visible below about 10 keV due to nuclear starburst activity (see, e.g., Schurch et al. 2002 and references therein). NGC 4945 required a high energy rollover at  $\sim 60$  keV for a good fit (see RMR2011 for more details on NGC 4945).

NGC 6240 has scattered nuclear emission below  $\sim 10$  keV found by Lira et al. (2002) using *Chandra*, with possible starburst contamination and a binary nucleus (Komossa et al. 2003).

NGC 6300 has been reported to have very interesting spectral behavior, changing from a reflection dominated to a regular Compton-thin Seyfert 2 (Leighly et al. 1999; Guainazzi 2002), while a variability study by Awaki et al. (2005) has indicated that it may be a Seyfert 1 core obscured by heavy absorption. However, the faintness of the source means that it has been difficult to properly constrain these models in order to test these ideas. With only 27 ks of data and a flux of  $\sim 6 \times 10^{-12}$  erg cm $^{-2}$  s $^{-1}$ , we are not able to constrain these models very well either. Fitting the data with a reflection-only model yields  $\chi^2/\text{dof} \sim 1$ , and  $\Gamma \sim 2.1$ , while a partial-covering Compton-thick absorber model with no reflection yields  $N_{\text{H}} \sim 3 \times 10^{24}$  cm $^{-2}$  and  $\chi^2/\text{dof} \sim 0.5$ . Neither of these is an improvement over our base model fit, but are plausible fits to the data.

NGC 7582 may also be reflection dominated, however it was not possible to disentangle the absorbed power law and the CRH for these sources. NGC 7582 has been modeled with very strong neutral reflection plus an underlying power or with a partial covering absorber of the continuum (Turner et al. 2000; Bianchi et al. 2007) and we find that modeling either of these components provided a good fit to our data. Note that if *RXTE* caught the source sometimes Compton-thick and sometimes Compton-thin (Piconcelli et al. 2007, Bianchi et al. 2009), then a partial covering absorber model would provide a good fit of the time-averaged data and would make it difficult to measure accurately the actual quantity of reflected emission.

For almost all of the blazars in our sample a simple or broken power law gave a good description of the spectrum, however 3C 273 is something of a special case with an Fe line and Compton hump having been detected previously in this source (e.g., Grandi et al. 1997, Kataoka et al. 2002). A Compton reflection component was significant to include at the 96% confidence level but with a very low value of  $R$  ( $0.04 \pm 0.03$ ) and it was significant to include an Fe line at only the 86% confidence level with an EW of  $50 \pm 40$  eV. This is consistent with a Seyfert-like source being diluted by the jet component in the X-ray band.

The blazars 1ES 1218+304 and Mkn 766 are located 0.73 degrees from each other. We therefore performed additional analysis to determine the level of contamination in each source. At this off-axis angle, the PCA response is  $\sim 21\%$ . We measure a 2–10 keV flux for Mkn 766 of  $2.7 \times 10^{-11}$  erg cm $^{-2}$  s $^{-1}$ , consistent with measurements many other X-ray missions (e.g., Ueda et al. 2001, Markowitz et al. 2007). Meanwhile, we measure a 2–10 keV flux for 1ES 1218+304 of  $1.2 \times 10^{-11}$  erg cm $^{-2}$  s $^{-1}$ ; previous 2–10 keV flux measurements span the range  $1.5$  to  $2.6 \times 10^{-11}$  erg cm $^{-2}$  s $^{-1}$  (from *BeppoSAX*: Giommi et al. 2005; *XMM-Newton*: Blustin et al. 2004; *Suzaku*: Sato et al. 2008). It is likely that the 1ES 1218+304 spectrum is contaminated at some level, but given the high variability of Mkn 766 we can only give a rough estimate of the exact amount of contaminating flux. *BeppoSAX* observed Mkn 766 in May of 1997,  $\sim 10$  days before the *RXTE* observations of 1ES 1218+304, and measured the 2–10 keV flux to be  $2.0 \times 10^{-11}$  erg cm $^{-2}$  s $^{-1}$  (Matt et al. 2000). This would correspond to a contaminating flux of  $\sim 0.4 \times 10^{-11}$  erg cm $^{-2}$  s $^{-1}$  in the 2–10 keV range, introducing systematic errors on the measurement of the photon index of  $\sim 0.1$  and on the overall flux at around the 30% level.